Progress in Radiology 2018

The 12th Symposium of the Japanese
Scandinavian Radiological Society (JSRS)
& the 15th Nordic Japan PACS Symposium

June 13-15, 2018
Bergen, Norway

Dear Friends,

It is our great pleasure to welcome you all to *Progress in Radiology 2018*, the 12th Symposium of the Japanese Scandinavian Radiological Society (JSRS) & the 15th Nordic Japan PACS Symposium.

Progress in Radiology 2018 aims to promote the exchange of scientifically based radiological skills and to build professional networks between Scandinavian and Japanese radiologists. The JSRS has a proud tradition having organized very successful previous symposiums and facilitated the exchange of radiological expertise between Japan and Scandinavia since JSRS's formal inception in 1986. The organizing committee has long been preparing this conference, hoping to succeed in hosting *Progress in Radiology 2018* in a similar collaborative and successful way as previous years. We have also included a session about "The JSRS – Its historic impact and future directions", hoping to promote discussions that may revitalize the society and secure its future relevance for Japanese and Scandinavian radiologists. The fact that *Progress in Radiology 2018* will have ~100 participants from Japan and Scandinavia this year, is very inspiring proving that this society is highly relevant for radiologists today.

The symposium will, similar to previous years, cover topics ranging from oncologic imaging, cardiovascular imaging, interventional radiology, breast imaging, nuclear medicine, neuroimaging, musculoskeletal and molecular imaging to PACS related topics. The scientific program is very much influenced by the submitted abstracts with a total of 51 accepted oral presentations and 12 poster presentations. Furthermore, presentations by primary investigators at the newly established Mohn Medical Imaging and Visualization Center (MMIV) in Bergen (www.mmiv.no) will be given, presenting projects that may be highly relevant for collaboration within SJRS.

The conference venue is Grand Hotel Terminus, a classic continental hotel and conference center beautifully located in downtown Bergen and within walking distance to some of the most famous sightseeing attractions in Bergen. The social program starts on June 13th with a hospital visit at Haukeland University Hospital, followed by sight-seeing in the vicinity of Bergen and a visit at Troldhaugen (the home of the composer Edvard Grieg) ending with a reception hosted by the mayor of Bergen in Håkonshallen in Bergen. On June 14th, after transportation with the funicular to Fløyen, the evening gala dinner is hosted in the historic Fløien Restaurant at Fløyen providing a spectacular view of Bergen and the harbor.

Progress in Radiology 2018 is organized in collaboration with The Norwegian Radiological Society, Mohn Medical Imaging and Visualization Center at Haukeland University Hospital and the University of Bergen. This conference has been generously supported by the Scandinavia-Japan Sasakawa Foundation – Norway and is sponsored by vendors who will present their latest state-of-the art imaging technologies at the conference.

We are honored to have been given the opportunity to host *Progress in Radiology 2018* in Bergen. We hope that you will find the conference rewarding, and that you enjoy your stay in Bergen.

Local organizing commitee

Ingfrid S. Haldorsen
President

Gesche Neckelmann

Jenny Husby

Aslak Aslaksen
(Head of Dep. Radiology)

Jens Prahl

Tore Bach-Gansmo
(Oslo Univ. Hospital)

Per-Kristian Hol
(Oslo Univ. Hospital)

Dep. of Radiology, Haukeland University Hospital/MMIV, Haukeland University Hospital / University of Bergen

PCO: Kongress & Kultur AS, Bergen KONGRESS & KULTUR

Wednesday June 13th

09.00-12.00	**Hospital visit at Haukeland University Hospital**
09.00	Pickup outside Grand Hotel Terminus
09.30-11.00	**Introduction to the Norwegian Public Health System and to the hospital- and imaging facilities at Haukeland University Hospital. Auditorium Central Building (H-113)**
09.30-09.50	Public Health System in Norway and History of Haukeland University Hospital (MD Gesche Neckelmann)
09.50-10.05	Imaging Facilities and Core Activities at Dep. of Radiology, Haukeland University Hospital (Head of Dep. of Radiology Aslak Aslaksen)
10.05-10.20	Imaging Facilities and Core Activities at the PET Centre, Haukeland University Hospital (Head of PET Centre, Nina Kleven Madsen)
10.20-10.30	**COFFEE BREAK**
10.30-11.00	Thyroid Cancer – Imaging markers for individualized treatment. Prof. Martin Biermann, Haukeland University Hospital
11.00-11.45	**Walk with visit at the PET Centre and at the Mohn Medical Imaging and Visualization Centre**
11.45	Return by bus to Grand Hotel Terminus
14.00-18.00	Guided **City Sightseeing** by bus, **Guided Tour** and **Concert at Edvard Grieg Museum**, **Troldhaugen**. The tour starts outside Grand Hotel Terminus and ends at Håkonshallen.
18.00	**Reception by the municipality of Bergen at Håkonshallen (with drinks and a light meal)**
19.00	**Walk** from Håkonshallen to the Grand Hotel Terminus past **Bryggen**

Thursday June 14th

08.00 *Registration and Coffee*

09.00-09.05 **Opening remarks by the President of *Progress in Radiology 2018* Ingfrid Haldorsen**

09.05-10.25 **Breast** (Moderators: Peter Dean and Hiroko Tsunoda)

09.05-09.15 Breast Cancer Tumor Features According to the Site of Origin: A descriptive classification with illustrative examples. Peter Dean, Turku, Finland

09.15-09.25 Digital breast tomosynthesis versus digital mammography: recall rate by mammographic density - interim analyses. Hildegunn Aase, Bergen, Norway

09.25-09.35 Prevalence of Mammographically Dense Breasts in Yamagata, Japan. Megumi Kuchiki, Yamagata, Japan

09.35-09.45 How Japan Handles Dense Breasts in Breast Cancer Screening. Hiroko Tsunoda, Tokyo, Japan

09.45-09.55 Diffusion-Weighted Whole-Body Imaging with Background Body Signal Suppression (DWIBS) Mammography for Screening Women with Dense Breasts: a Feasibility Study. Takayoshi Uematsu, Shizuoka, Japan

09.55-10.05 Sonographic features can predict pathological response to neoadjuvant chemotherapy among triple-negative and HER2-positive breast cancer. Tomohiro Ochi, Tokyo, Japan

10.05-10.15 Long-term outcomes in patients treated with whole-breast irradiation after breast-conserving surgery, Yoshio Monzen, Nagasaki, Japan

10.15-10.25 Readout-segmented echo-planar diffusion-weighted images during breast magnetic resonance imaging: a clinical application. Satoshi Honda, Tokyo, Japan

10.25-10.45 *Coffee break in the exhibition area*

10.45-11.45 **Precision Imaging Initiative at Mohn Medical Imaging and Visualization (MMIV) Center Relevant for JSRS** (Moderators: Aslak Aslaksen and Tetsuhisa Yamada)

10.45-11.00 Renate Grüner: “Precision imaging in neurologic disease”

11.00-11.15 Arvid Lundervold: “Machine Learning for Precision Imaging”

11.15-11.30 Ingfrid Haldorsen: Precision Imaging in Gynecologic Cancer

11.30-11.45 Noeska Smith: Precision imaging in rectal cancer

11.45-12.00 **Latest state of the art imaging technology by Nordic NeuroLab**

12.00-13.00 *Lunch in restaurant followed by exhibition/poster discussion*

13.00-14.20 **Abdominal and cardiac/chest imaging** (Moderators Kazunori Kuroki and Anselm Schultz)

13.00-13.10 From Gd-EOB-DTPA-enhanced liver MRI with global liver function evaluation. Nils Dahlstrøm, Linkøping, Sweden.

13.10-13.20 MRI assessed tumor free distance to serosa predicts deep myometrial invasion and poor prognosis in EC. Julie Andrea Dybvik, Bergen, Norway

13.20-13.30 Pancreatic fatty infiltration at Dixon-MRI is a marker of exocrine pancreatic insufficiency in cystic fibrosis (CF) - a comparison of pancreatic echogenicity at US and pancreatic fat content by MRI. Giedre Kavaliauskiene, Oslo, Norway

13.30-13.40 Imaging features of adnexal torsion. Aya Yamane, Kanagawa, Japan

13.40-13.50 High abdominal fat content and high visceral fat proportion are associated with advanced FIGO stage in endometrial cancer. Kristine Fasmer, Bergen, Norway

13.50-14.00 Efficacy of Adrenal Venous Sampling in Primary Aldosteronism. Soma Kumasaka, Gunma, Japan

14.00-14.10 Effect of the left atrial diameter on the quality image in coronary computed tomography angiography (CCTA). Tien Nguyen-Cong, Gunma, Japan

14.10-14.20 Improved three-dimensional CT image quality of high contrast anatomies with an ultra-high-resolution CT scanner: initial clinical experience. Haruhiko Machida, Tokyo, Japan

14.20-15.00 *Coffee break in the exhibition area*

15.00-16.00 **Neuroimaging** (Moderators: Gesche Neckelmann and Takaaki Hosoya)

15.00-15.10 Magnetic resonance imaging of the neck in patients presenting symptoms of neck infection in an emergency setting. Janne Nurminen, Turku, Finland

15.10-15.20 Methodological considerations in designing olfactory fMRI studies. Charalampos Georgiopoulos, Linkøping, Sweden

15.20-15.30 CT baseline findings that predict progressive paranasal sinus disease in granulomatosis with polyangiitis. Sigrun Skaar Holme, Oslo, Norway

15.30-15.40 Longitudinal stability of the brain functional connectome is associated with episodic memory performance. Olga Therese Ousdal, Bergen, Norway

15.40-15.50 A population study of Norwegian psychiatric patients referred for clinical brain scanning. Mona Beyer, Oslo, Norway

15.50-16.00 Multi-b-value, multi-echo characterization of water diffusion within infarcted tissue. Leif Oltedal, Bergen, Norway

16.00-17.00 **The Japanese Scandinavian Radiological Society (JSRS) - Historic impact and future directions.** Moderators: Prof Ingfrid Haldorsen, Prof. Tetsuhisa Yamada (former President of «Progress in Radiology 2016)

Historic impact of JSRS for the exchange of scientifically based radiological skills and building professional networks amongst:

16.00-16.10 Japanese Radiologists (Professor Hiroyuki Tajima, President Japanese Board of JSRS, Nippon Medical School)

16.10-16.20 Scandinavian Radiologists (Professor Frode Lærum former President of "Progress in Radiology" in Oslo in 2001)

Future directions of JSRS to increase the potential impact of the society in years to come:

16.20-16.30 Perspectives from Japan. Professor Masamitsu Hatakenaka, President of «Progress in Radiology 2020"

16.30-16.40 Perspectives from Scandinavia. Professor Jarmo Reponen, Vice President of "Progress in Radiology 2014"

16.40-17.00 Plenary discussion

Social program

19.00-22.30 Conference dinner at Fløyen

For those who want to walk directly from Hotel Terminus to Fløibanen (the funicular), we will leave from the reception at Hotel Terminus at 18:30.

Friday June 15th

08.00-08.45 **International Board Meeting**

08.45-09.45 **Oncologic Imaging** (Moderators: Rimma Axelson and Yoshio Monzen)

08.45-08.55 Preoperative tumor texture analysis on MRI predicts high-risk disease and reduced survival in endometrial cancer, Sigmund Ytre-Hauge, Bergen, Norway

08.55-09.05 ADC value negatively correlates to regional pathological grades of uterine endometrioid carcinoma. Maki Onodera, Sapporo, Japan

09.05-09.15 ADC calculated with b-values of 0 and 1500 sec/mm2 would be superior to that with 100 and 1000 sec/mm2 in prostate cancer. Masamitsu Hatakenaka, Sapporo, Japan

09.15-09.25 Can 18F-FDG PET predict the response to 131I radioactive iodine ablation therapy in metastatic differentiated thyroide carcinoma? Xieyi Zhang, Gunma, Japan

09.25-09.35 FDG-PET/CT evaluation of histological response after neoadjuvant treatment in patients with cancer of the oesophagus or gastroesophageal junction. Stefan Gabrielson, Stockholm, Sweden

09.35-09.45 Entropy from Preoperative CT Texture Analysis – A Potential Imaging Biomarker for Early Recurrence after Resection of Colorectal Liver Metastases. Anselm Schultz, Oslo, Norway.

09.45-10.00 **Latest state-of-the-art imaging technology by Sectra Medical Education and Training**

10.00-10.15 Coffee break in the exhibition area

10.15-11.45 **Intervention** (Moderators: Hiroyuki Tajima and Mona Beyer

10.15-10.25 Transvenous Coil Embolization for a Dural Arteriovenous Fistula with Angiographically Isolated Transverse-Sigmoid Sinus: Multiple Microcatheter Technique via a Modern Triaxial System. Takahiko Mine, Copenhagen, Denmark

10.25-10.35 C-Arm Cone-Beam CT-guided needle biopsies with prone position through the erector spinal muscle for posterior thoracic pulmonary nodules. Nobuyuki Takeyama. Yokohama, Japan

10.35-10.45 Clinical Assessment of Interventional Radiology for the Treatment of Acute Venous Thromboembolism. Hiroyuki Tajima, Kawasaki, Japan

10.45-10.55 Wide-necked Renal Saccular Artery Aneurysms: Long-term outcome of balloon assisted coil embolization. Tetsuhisa Yamada, Tokyo, Japan

10.55-11.05 Endovascular Treatment of Type Ia Endoleak Using N-butyl Cyanoacrylate Embolization and Proximal Cuff Placement. Akio Kotake, Yokohama, Japan

11.05-11.15 Percutaneous intervention for tricuspid valve vegetation under intracardiac echocardiographic guidance. Daisuke Yasui, Tokyo, Japan

11.15-11.25 Balloon-assisted transcatheter arterial n-butyl cyanoacrylate embolization of femoral artery bleeding. Tatsuo Ueda, Tokyo, Japan

11.25-11.35 Efficacy and safety of transcatheter arterial embolization with N-butyl Cyanoacrylate for acute lower gastrointestinal bleeding. Izumi Tanaka, Tokyo, Japan

11.35-11.45 Changes in aortic wall thickness related to onset of acute aortic dissection on contrast enhanced computed tomography. Hidemaso Saito, Tokyo, Japan

11.45-12.00 **Latest state-of-the-art imaging technology by Siemens**

12.00-13.00 *Lunch in the exhibition area with sponsors/vendors*

13.00-13.40 **PACS/informatics and education** (Moderators: Finn Mathiesen and Anders Persson)

13.00-13.10 European Training Assessment Program (ETAP 2.0) in Radiology. Hannu Aronen, Turku, Finland

13.10-13.20 Integration of medical imaging storages using a patient-based PACS system. Takahito Nakajima, Gunma, Japan

13.20-13.30 PACS is coming to the era of cloud storage. Hioshi Kondah, Yonago, Japan

13.30-13.40 Semiautomated segmentation of body composition in abdominal CT images using SliceOmatic – Inter- and intraobserver variation. Lisa J Kjoenigsen, Oslo, Norway

13.40-14.40 **Musculoskeletal radiology and miscellaneous** (Moderators: Jenny Husby and Hiroshi Kondo)

13.40-13.50 Extra-osseous uptake of bone scintigraphic agent DPD. Tore Bach-Gansmo, Oslo, Norway

13.50-14.00 Diagnosis of peri-prosthetic infection at the hip using standard uptake value of 99mTc-bone SPECT. Naoya Yama, Sapporo, Japan

14.00-14.10 KORTUC for lytic bone metastasis. Shiro Obata, Nagasaki, Japan

14.10-14.20 Future perspectives in quantitative forensic radiology. Anders Persson, Linkøping, Sweden

14.20-14.30 Incident/Accident Reports in the Radiology Department of Gunma University Hospital. Kazuhiro Kishi, Gunma, Japan

14.30-14.40 Evaluation of eye lens dose for percutaneous coronary intervention. Yuko Seki, Gunma, Japan

14.40-15.00 *Coffee break in the exhibition area*

15.00-15.40 **Nuclear Medicine** (Moderators: Hannu Aronen and Tore Bach-Gansmo)

15.00-15.10 68Ga-PSMA PET/CT- a magic bullet? Rimma Axelsson, Stockholm, Sweden

15.10-15.20 Introduction to opportunistic screening using 3T PET/MR. Eriko Maeda,Tokyo, Japan

15.20-15.30 A single comparison of diffusion-weighted whole body MRI with background body signal suppression (DWIBS) and FDG-PET/CT for the renal pelvic cancer. Tsuyoshi Yoshida, Fukuoka, Japan

15.30-15.40 Analysis of GBCAs Deposition Mechanism by HPKC tandem ICP-MS in Mice Following Single Dose Administration. Putri Andriana, Gunma, Japan

15.40-16.00 Closing remarks by Ingfrid Haldorsen and Masamitsu Hatakenaka

Progress in Radiology 2018 is organized under the auspices of MMIV, Haukeland University Hospital and University of Bergen and is sponsored by:

Scandinavia-Japan Sasakawa Foundation – Norway
Nordic NeuroLab
Siemens Healthineers
Sectra
Vingmed
GE Healthcare
Phillips

SOCIAL EVENT JUNE 13th

Opening reception in Håkonshallen at 18:00

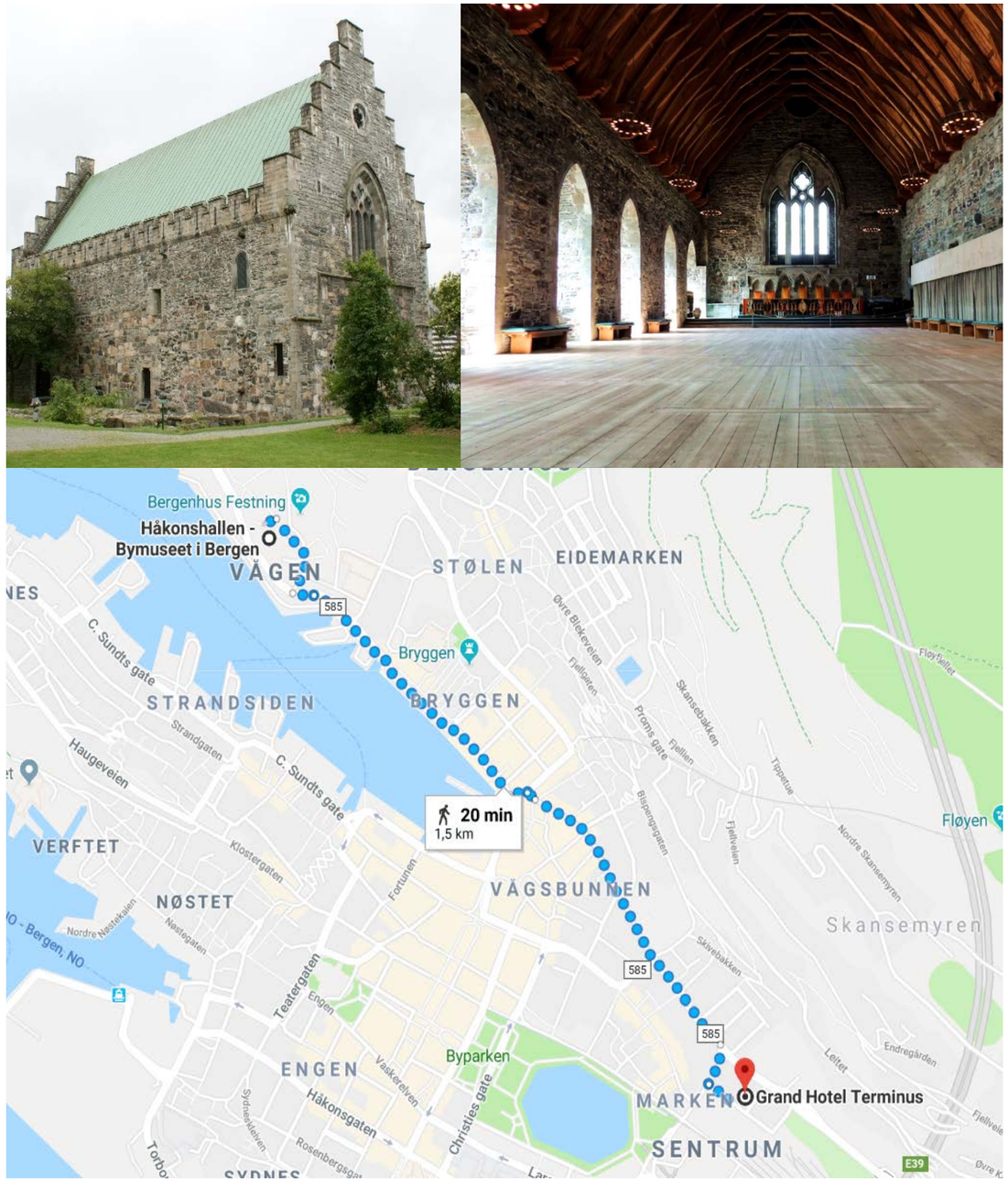

Scenic walk past Bryggen from Håkonshallen to Hotel Terminus

SOCIAL EVENT JUNE 14th

Conference dinner at Fløien Restaurant at 19:00

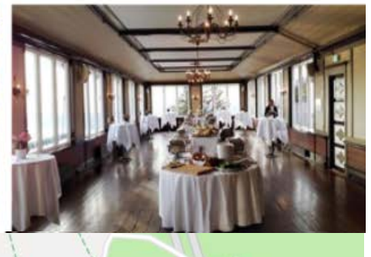

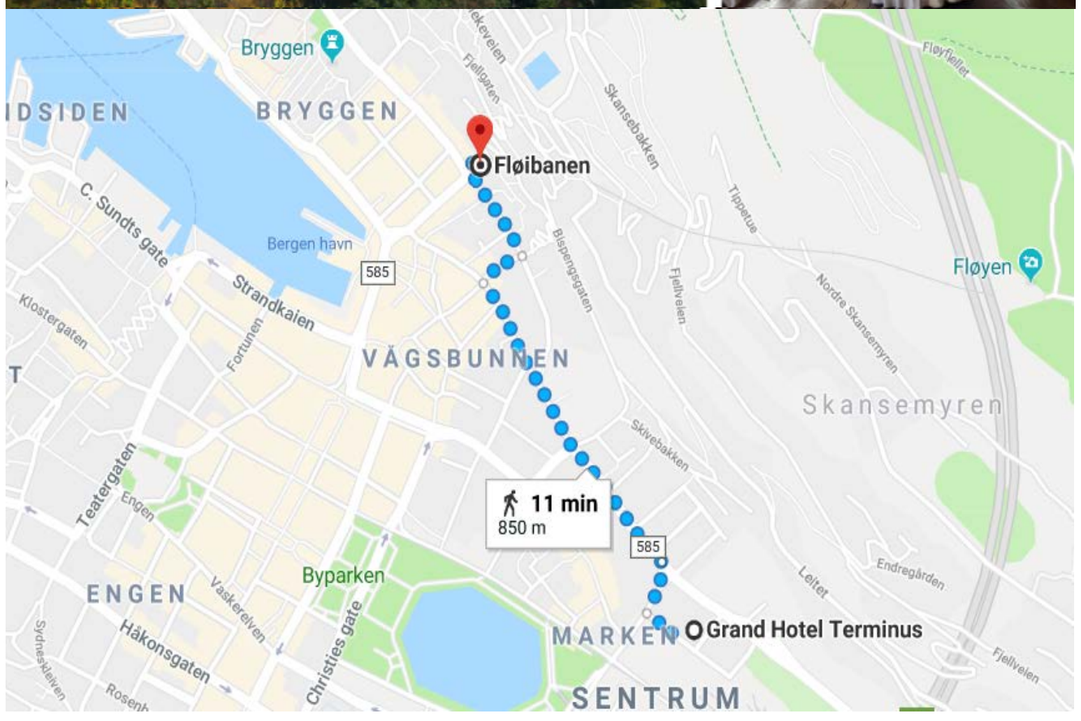

Walk from Hotel Terminus to Fløibanen (the funicular leaves every 15 minutes from 10:00-19:00, and every 30 minutes from 19:00-23:00).

THURSDAY JUNE 14th 09.05-10.25

Breast

Moderators: Peter Dean and Hiroko Tsunoda

8 presentations

Breast Cancer Tumor Features According to the Site of Origin: A descriptive classification with illustrative examples

László Tabár and Peter B. Dean, Finland

Breast cancer management is based on the tumor type, grade, extent, node status and more distant metastases. Radiologists and pathologists work together to estimate the tumor extent preoperatively in order to help the surgeons successfully remove the entire malignancy on the first operation. Unfortunately, the pathology nomenclature we have inherited is an impediment to successful interdisciplinary cooperation, as some of the terms used by pathologists are conflicting and frequently misunderstood by other colleagues. The classification of widely differing malignancies under a common name inhibits progress in individual-based diagnosis and treatment, and is a situation which should be remedied. To help overcome this problem, a new classification based on the site of origin of breast cancers, as determined from subgross, large section, three-dimensional breast pathology with imaging correlation, has been developed, and will be presented along with detailed illustrative examples.

Digital breast tomosynthesis versus digital mammography: recall rate by mammographic density - interim analyses

Hildegunn S Aase, Åsne S Holen, Berit Hanestad, Ingfrid S Haldorsen, Solveig Hofvind

Purpose: To compare doses and recall rates using synthetic mammography + digital breast tomosynthesis (SM+DBT) versus digital mammography (DM) in the Norwegian Breast Cancer Screening Program, stratified by mammographic density.
Methods and Materials: As part of a randomized controlled screening trial performed in Bergen, 7037 women were screened with SM+DBT and 7052 with DM, January-December 2016. We obtained doses and continuous measures of volumetric breast density (VBD) using an automated software (Volpara version 1.5.1). Doses for all screened women, and recall rate for positive mammographic findings was calculated for women who underwent screening with the two techniques, recall rates were stratified by quartiles of VBD; (1: <3.5%; 2: 3.5-5.4%; 3: 5.4-8.8% and 4: >8.8%). Two-proportion z-tests was used to test for statistical significance between the groups ($p<0.05$).
Results: Mean radiation-dose per examination/per breast was for DM 2.95 mGy, and for DBT 2.96 mGy, $p=0.43$. Recall rate was statistically significantly lower for SM+DBT (3.0% [208/7037]) compared to DM (3.6% [254/7052], $p=0.03$). The recall rate increased by mammographic density for SM+DBT, from 2.1% for VBD-1 to 4.5% for VBD-4. For DM, the recall rate remained the same for different quartiles of mammographic density. For DM, the highest recall rate (4.3%) was observed for VBD-3.
Conclusion: Radiation-doses were close to equal in the two arms. Women screened with SM+DBT had a lower recall rate compared to those screened with DM. The higher recall rate among women with dense breast and screened with SM+DBT need to be followed closely according to cancer detection and rate of false positive screening results.

Prevalence of Mammographically Dense Breasts in Yamagata, Japan

Megumi Kuchiki &Takaaki Hosoya. Yamagata, Japan.

Background: Mammographically dense breasts currently represent one of major topics in breast cancer screening in Japan. In the United States, disclosure of mammographic breast density (MBD) information directly to women with dense breasts is mandated, and this legislation has had a considerable impact on breast cancer screening in Japan. However, there currently exist no global guidelines for dense breasts, and the number of Japanese women potentially affected is unclear.

Purpose: To determine the prevalence of dense breasts in Yamagata, Japan, and discuss the possibility of notifying MBD information to women and conducting supplemental breast cancer screening by ultrasound (US).

Materials and Methods: We determined the prevalence of dense breasts using data from 49973 mammograms from April 1, 2016 to March 31, 2017 in Yamagata, Japan. Board-certificated radiologists qualitatively rated MBD according to four categories defined by the 5th edition of the American College of Radiology Breast Imaging Reporting and Data System (BI-RADS). We also surveyed the number of board-certificated medical doctors and breast screening radiographers/sonographers in mammography/US.

Results: Overall, 39.5% of women aged 30 to 79 years had heterogeneously or extremely dense breasts. There was a significant inverse relationship between age and breast density (P<0.001). Among women with dense breasts, 66.5% were in their 30s, 57.1% were in their 40s, 40.6% were in their 50s, 27.5% were in their 60s, and 17.5% were in their 70s. Roughly 20,000 women aged 30 to 79 years were estimated to have heterogeneously or extremely dense breasts in Yamagata. There were 118 board-certificated medical doctors and 115 radiographers in mammography, and 5 doctors and 9 sonographers in US. It showed absolutely short of the numbers in US compared to in mammography.

Conclusion: Roughly 20,000 women in Yamagata are estimated to have dense breasts. Our findings suggested that notifying MBD information to women, and conducting supplemental breast cancer screening by US, are currently difficult. Policymakers should consider the high prevalence of dense breasts when debating breast density notification and designing strategies to ensure that women who are notified have opportunities to pursue supplemental screening options.

How Japan Handles Dense Breasts in Breast Cancer Screening

Hiroko Tsunoda*1,2, Yoshio Kasahara*1,3, Akihiko Suzuki*1.4, Hirokazu Takahashi*1,5, Takayoshi Uematsu*1,6,

*1 Dense Breast Working Group, *2 Depart. of Radiology St Luke's International Hospital, *3 Vice Director ,Fukui Prefecture-Saiseikai Hospital, *4 Department of Breast and Endocrine Surgery, Tohoku Medical and Pharmaceutical University, *5 Cancer Screening Management Section, Division of Cancer Screening Assessment and Management, Center for Public Health Science, National Cancer Center, *6 Department of Breast Imaging and Breast Intervention, Shizuoka Cancer Center Hospital

Background: In Japan, mammography screening for women over 50 years of age was instituted starting in the year 2000. From 2004, the screening age was expanded to include women above 40. The screening results are relayed to women in terms of either necessity for further examination or not. While it is known that the detection rate of breast cancer is low in dense breasts, the finding of breast composition is not normally relayed to women undergoing screening. In the United States, in contrast, the "Are you dense?" campaign was introduced with mandatory notification regarding the breast composition found at mammography screening. Subsequently, this campaign and the limits of breast cancer detection in dense breasts were featured by the Japanese mass media in 2016. In response, some measures were instituted.

Activity content: In 2016, the Dense Breast Working Group was launched and to investigate issues related to dense breasts. First, the group defined what is meant by a "dense breast". In Japan, breasts were previously classified into the four groups of "fatty", "scattered", "heterogeneously dense", and "dense"; the group decided to define a "dense breast" as either being what was previously classified as a "heterogeneously dense" or "dense" breast. When starting mammography screening, Japan established the Japan Central Organization on Quality Assurance of Breast Cancer Screening, held a mammography workshop, created a certification system for interpreting doctors, and implemented quality control. It was found that the evaluation of the breast composition was quite different between observers. Also, Japan has large regional differences in manpower and knowledge and education about dense breasts are lacking. In addition, when a dense breast is diagnosed, clinicians do not know the appropriate next step. Therefore, at present, it was deemed to be premature to establish nation-wide notification requirements for women about their breast composition. Rather, notification of the breast composition is planned to be implemented after establishing a system in which study progression (e.g. examination modality, etc.) is clearly delineated.

Diffusion-Weighted Whole-Body Imaging with Background Body Signal Suppression (DWIBS) Mammography for Screening Women with Dense Breasts: a Feasibility Study

Takayoshi Uematsu. MD and PhD
Department of Breast Imaging and Intervention
Shizuoka Cancer Center Hospital
Japan

Purpose: To evaluate clinical feasibility of diffusion-weighted whole-body imaging with background body signal suppression (DWIBS) mammography for detecting mammographically occult breast cancer in women with dense breasts, and develop assessment criteria for the binary management decision: recall or not.

Materials and Methods: Three hundred thirty patients with 360 lesions, including 34 mammographically occult breast cancers, 279 mammography detected breast cancers, and 47 benign lesions, were examined with DWIBS and short T1 inversion recovery (STIR) using 3 T MRI at b values of 0 and 1,000 s/mm^2. The scanning time was 8 minutes and 20 seconds. Mammographically occult breast cancers were evaluated for visibility on DWIBS mammography and the reading time was measured, then the signal and morphology on STIR were compared with breast cancers and benign lesions. DWIBS mammography was displayed as an inverted grey scale maximum intensity projection. A lesion detected on DWIBS mammography was considered positive if it showed low signal intensity relative to the background breast parenchyma.

Results: DWIBS mammography sensitivity for mammographically occult breast cancer was 91% and the average reading time was 11 seconds. Low/iso intensity on STIR ($p<0.0001$), non-mass lesion type ($p<0.026$), and ill-defined margin ($p<0.0001$) were significantly associated with breast cancer.

Conclusion: Unenhanced DWIBS mammography with STIR image has high sensitivity for mammographically occult breast cancer with the shorter scanning time and faster reading time; these results suggest that this technique might be useful as a supplemental screening modality for women with dense breasts. A unique area of low signal intensity on DWIBS mammography and low/iso on STIR should be recalled, especially with ill-defined margin.

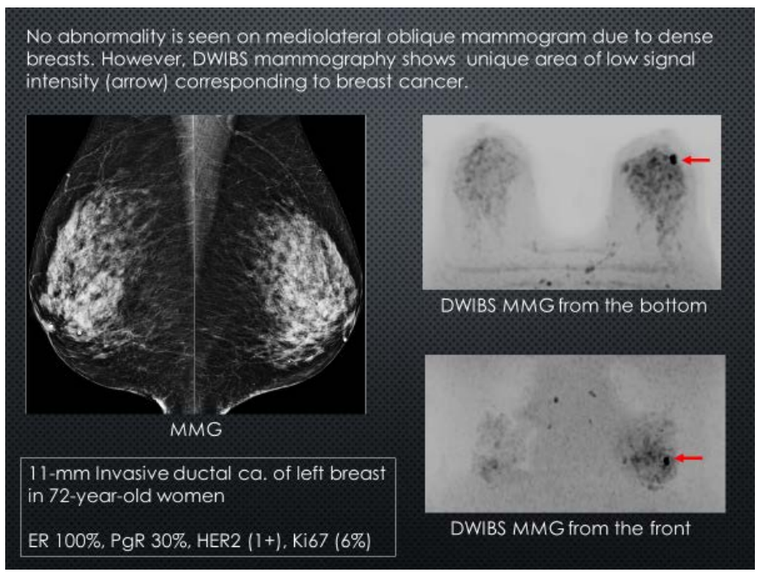

Sonographic features can predict pathological response to neoadjuvant chemotherapy among triple-negative and HER2-positive breast cancer

Tomohiro Ochi[1], Hiroko Tsunoda[2], Naoko Matsuda[1], Emiko Morishita[2], Fumi Nozaki[3], Kouyu Suzuki[3], Yuki Yonekura[4], Hideko Yamauchi[1]

Departments of [1]Breast Surgical Oncology, [2]Radiology, and [3]Pathology, St. Luke's International Hospital, Tokyo, Japan, and [4] Department of Nursing Informatics, Graduate School of Nursing Science,
St. Luke's University, Tokyo, Japan

Abstract

Introduction: Response to neoadjuvant chemotherapy (NAC) is associated with the prognosis of primary breast cancer patients. Some articles have reported that patients who achieved pathological complete response (pCR) have higher disease-free survival rate than those with non-pCR in triple negative breast cancer (TNBC), and HER2-positive breast cancer. We aimed to predict pCR to NAC, using ultrasonography (US). We focused on the characteristics in size and echogenicity of each tumor among TNBC and HER2 positive breast cancers.

Methods and materials: A total of 83 patients, constituting 51 TNBC and 32 HER2-positive ER-negative patients, who received NAC and surgical treatment between January 2015 and December 2016, were included in this study. Patients with inflammatory breast cancer, breastfeeding breast cancer, stage IV breast cancer, large tumors beyond the width of the probe, and sonographically invisible tumors were excluded from this study. We retrospectively determined the clinicopathological characteristics in size and echogenicity of the tumor. All patients had undergone US after NAC. We measured the depth and width of the tumors. A representative region of interest (ROI) was chosen from the tumor (T) and the fat (F) regions, and the brightness of each region was measured. The ratio of echogenicity (T/F ratio) was then determined by dividing the numerical measurements of the brightness at the ROI of the tumor, by the brightness at the ROI of the fat region. We compared the T/F ratio of the pCR (ypT0/is, ypN0) and non-pCR patients.

Results: pCR was achieved in 19 (37.3%) of the 51 TNBC cases and 19 (59%) of the 32 HER2-positive cases. The T/F ratio after NAC was significantly associated with pCR. pCR cases showed higher T/F ratio compared to non-pCR cases ($p=0.022$). As we analyzed its subgroup characteristics, we observed that TNBC showed the tendency to have higher T/F ratio statistically ($p=0.012$), but HER2 type did not ($p=0.644$). Moreover, the TNBC subtype showed a statistically significant shrinkage of the depth ($p=0.042$) and width ($p=0.018$) of the tumor, while the HER2-positive subtype showed a slight but statistically insignificant shrinkage of the tumor's depth ($p=0.109$), but not of its width ($p=0.463$).

Conclusion: TNBC and HER2-positive breast cancers have different sonographic features after NAC. These features may be utilized to predict pCR among TNBC.

Long-term outcomes in patients treated with whole-breast irradiation after breast-conserving surgery

Authors: Yoshio Monzen, Masahide Mutsukura, Masayuki Baba, Shinsuke Hara.
Sasebo City General Hospital, Nagasaki, Japan

Objective: The long-term outcomes of whole-breast irradiation (WBI) after breast-conserving surgery (BCS) for patients with breast cancer were retrospectively analyzed.
Materials and Methods: From 2000 to 2010, 326 breast cancer patients who underwent BCS followed by WBI were analyzed. The median doses of WBI and boost irradiation were 50 Gy in 25 fractions (range, 42.6 Gy-50 Gy) and 10 Gy in 5 fractions (range, 0-10 Gy), respectively. The median follow-up time was 113 months (range, 27-199 months).
Results: Nine patients (2.8%) died of breast cancer, and 11 patients (3.4%) died of other diseases. The 10-year overall survival, cause-specific survival, and disease-free survival rates were 94.2%, 96.8%, and 84.9%, respectively. Local recurrence was observed in 17 patients (5.2%). The cumulative incidence of local recurrence was 2.4% and 5.1% at 5 and 10 years, respectively. First-time distant metastasis occurred in 17 patients (5.2%). Metachronous secondary cancer occurred in 34 patients (10.4%). The frequency of endometrial cancer and colon cancer was high, except for patients with metachronous contralateral breast cancer. There was no significant difference in the local recurrence rate between T1 and T2 or between N0 and N1. The frequency of distant metastasis in T1 and N0 was lower than that in T2 and T4 and N1 and N2, respectively.
Conclusion: The treatment results of breast-conserving therapy were favorable. Seven patients died of metachronous secondary cancer among 11 patients who died of other diseases. We must consider the occurrence of metachronous secondary cancer in the follow-up of these patients.

Readout-segmented echo-planar diffusion-weighted images during breast magnetic resonance imaging: a clinical application

Satoshi Honda, Yukino Kozuka, Toshiyuki Onodera and Yoichi Okada
Tokyo Metropolitan Health and Medical Treatment Corporation, Toshima Hospital, Department of Radiology

Purpose: Diffusion-weighted image (DWI) is helpful in the detection of breast cancer, especially when background parenchymal enhancement is moderate or marked. DWI was used to assess the single-shot echo-planar (SS-EPI) technique. This technique yields distorted images during breast examination because the breast is an organ on the outside of the body and is surrounded by air. Currently, the magnetic resonance (MR) scanner produces DWI using the readout-segmented echo-planar imaging (RESOLVE) technique, which is known to reduce image distortion. We examined the clinical usefulness of DWI produced using the RESOLVE compared with SS-EPI techniques.
Subjects and method: We used a 1.5T MR scanner (Magnetome Aera, Siemens) with a 4-channel breast coil. Twenty breast cancer patients who underwent MRI at our hospital were investigated retrospectively. For ten patients, the SS-EPI technique was used, while the RESOLVE technique was used for the remaining ten patients. We compared hyperintensity on DWI and contrast enhancement on enhanced T1-weighted images (T1WI), produced using both techniques for the same lesion. Some examinations included multiple lesions.
Result: We measured the distance of the same lesion between the position of hyperintensity area on DWI and the corresponding part of contrast enhanced T1 WI. It was 3.3 ± 2.2mm in SS-EPI and 1.4 ± 1.1mm in RESOLVE. The DWI produced using the SS-EPI technique showed no lesions, which completely provided an overview of the same location on DWI and enhanced T1WI. However, the DWI produced using the RESOLVE technique showed some lesions in the same location in both DWI and enhanced T1WI.
Conclusions: DWI produced using the RESOLVE technique shows less distortion than that produced using the SS-EPI technique. These DWI produced using the RESOLVE technique allows easy comparison and localization of lesions in enhanced T1WI.

THURSDAY JUNE 14th 10.45-11.45

Precision Imaging Initiative at Mohn Medical Imaging and Visualization (MMIV) Center Relevant for JSRS

Moderators: Aslak Aslaksen and Tetsuhisa Yamada

Precision imaging in neurologic disease
Renate Grüner, MMIV Centre and UiB

In December 2017 a novel research centre the «Mohn Medical imaging and Visualization» was formally opened at the Department of Radiology, Haukeland University Hospital, Bergen, Norway. The Centre is established in collaboration between the University of Bergen and Haukeland University Hospital through financial support from the Bergen Research Foundation to promote cross-disciplinary research activities related to state-of-the art imaging equipment such as preclinical and clinical high field MRI, CT and hybrid PET/CT/MR. The aim of the Centre is to research new methods in quantitative imaging and interactive visualization to predict changes in health and disease across spatial and temporal scales. To date, three core research projects in artificial intelligence/ deep learning, medical visualization and cancer imaging, respectively, have been initiated as part of the Centre. In the current talk, research aims of a novel forth Centre project – Advanced NeuroImaging – will be presented.

Renate Grüner is the leader of the new Mohn Imaging and Visualization Centre (https://mmiv.no). She is also the co-leader of the Bergen fMRI group (https://www.uib.no/en/rg/fmri) – a neuroimaging research group repeatedly rated as "EXCELLENT" by the Norwegian Research Council. For two decades, Grüner has been involved in research and clinical neuroimaging, with a particular focus on MRI. Being trained as a physicist, she has an enthusiasm for methodological advances in the field and aims at investigating approaches for feature detection, feature extraction and feature prediction across CNS abnormalities. For more than ten years, Grüner has been teaching and supervising students in medical physics at the University of Bergen where she also holds a position as Associate Professor.

Machine Learning for Precision Imaging
Arvid Lundervold, MMIV Centre, Haukeland University Hospital/UiB

Machine learning (ML) aims to construct “programs or systems that builds and trains predictive models from input data, and uses the learned models to make useful predictions from new (previously unseen) data, drawn from the same distribution as the one used to train the models”. In this talk I'll put ML in the context of computational imaging and precision medicine (“integrating detailed information from multiple sources in a holistic manner”), focusing on morphological and functional MRI. Examples from previous and ongoing research in the ML-project at the MMIV Centre will be given. E.g. automated tissue classification in multispectral brain MRI, fast segmentation of brain and kidney using deep convolutional neural networks and transfer learning (joint with Alexander S. Lundervold), coregistration of histology and multiparametric MRI for the use of ML in prostate cancer, and application of ML in predicting irritable bowel syndrome (IBS) from multimodal brain MRI, addressing the brain-gut interaction in functional gastrointestinal disorders. Finally, I'll present some thoughts regarding future opportunities and challenges of (bio)medical imaging and machine learning for precision medicine.

Arvid Lundervold, BSc, MD, PhD is a professor in medical information technology and physiology at the University of Bergen, Norway. He is leading the Neuroinformatics and Image Analysis Laboratory in The Neural Networks Research Group (https://www.uib.no/en/rg/neuronet), Department of Biomedicine, and is PI (“Computational medical imaging and machine learning - methods, infrastructure and applications”) at the Mohn Medical Imaging and Visualization Centre (https://mmiv.no), Department of Radiology, Haukeland University Hospital. His current research interests are in the fields of medical image processing and pattern recognition; multimodal and functional imaging (in brain, kidney and in oncology); image segmentation; image registration; longitudinal imaging; imaging-based biomarkers; mathematical and statistical modeling including machine learning. Contact information at https://www.uib.no/en/persons/Arvid.Lundervold.

Precision imaging in gynecologic cancer
Ingfrid Haldorsen, MMIV Centre, Haukeland University Hospital/UiB

Gynecologic cancers have characteristic structural and functional imaging features reflected in clinical phenotypes, and these imaging biomarkers highlight pathogenic mechanisms potentially targetable by novel treatments. The challenge is now to integrate these imaging biomarkers into clinically relevant treatment algorithms by identifying molecular targets for treatment based on imaging biomarker profiles. Our multidisciplinary research team with competency in computer science, visualization and machine learning algorithms, diagnostic radiology, clinical gynecology, preclinical models and molecular biology/genetics will pursue these challenges as one of the funded projects within Centre for Medical Imaging and Visualization in Bergen.

Molecular and imaging biomarkers in gynecologic cancer will be studied in patients and in preclinical gynecologic cancer models. Potential imaging biomarkers will be identified using machine learning algorithms applied to multiparametric and functional magnetic resonance imaging (MRI) and positron emission tomography/computed tomography (PET/CT) from patients and in mouse models during therapy. Furthermore, the molecular and genetic alterations in the tumors as well as clinical phenotype and survival will be studied in relation to the corresponding imaging biomarker profile using integrative analyses. This provides a unique platform for identifying promising molecular targets for treatment and their corresponding imaging biomarker profiles. Studying imaging biomarkers in mice during targeted therapy will also facilitate the integration of imaging biomarker guided treatment algorithms and imaging guided monitoring of treatment response in gynecologic cancer. This project aims to improve patient care by enabling individualized and targeted treatment in gynecologic cancer patients.

Professor Ingfrid Haldorsen, MD and radiologist, has mostly been working with gynaecologic and abdominal imaging. Professor Haldorsen heads *Bergen Abdominal Research Group* (http://www.uib.no/en/rg/abdimaging) employing advanced imaging studies in abdominal disease and in cancers. Haldorsen also heads the Imaging Node of *Bergen Gynaecologic Cancer Research Group* and is heading the recently funded project: *“Precision Imaging in Gynaecologic Cancer”* within the Mohn Medical Imaging and Visualization Centre (http://mmiv.no/centre-project-2). She is an appointed working-group member of the Nordic Society of Gynecologic Oncology (NSGO) and in the Norwegian Directorate of Health. Haldorsen is an internationally recognized authority in radiology, illustrated by several invited review articles published in highly prestigious journals e.g. **Lancet Oncology, Nature Reviews Endocrinology** and **American Journal of Neuroradiology.** So far her mentoring, past and present, includes 8 PhD students and 2 post-doctoral fellows, and she is involved in high-profile local, national and international research collaboration in Europe, North America and Asia. Contact info: http://www.uib.no/personer/Ingfrid.S.Haldorsen.

Visualization for Precision Imaging in Rectal Cancer
Noeska Smit, MMIV Centre, Haukeland University Hospital/UiB

In medical visualization, computer-based interactive visual representations of medical (imaging) data are made, often aiming at improved diagnosis, treatment planning, treatment guidance, and/or doctor-patient communication. At times, there are structures that are not visible in the original medical imaging scans due to their limited size or image contrast with surrounding tissues. An example of this are the autonomic nerves surrounding the rectum, which are not visible in pre-operative MRI scans or during surgery. In this talk, I will present several examples of my research, aiming at enhancing medical imaging data by integrating information from various sources into a combined interactive visualization application for surgical planning and education purposes.

Noeska Smit is an Associate Professor in Medical Visualization at the University of Bergen, Norway. Her main affiliation is with the Visualization Group at the Department of Informatics, and she is also associated with the Mohn Medical Imaging and Visualization Centre at the Department of Radiology, Haukeland University Hospital. Noeska's has a mixed background in that she is a licensed radiographer, as well as obtained a PhD in Computer Science from the Delft University of Technology in the Netherlands. Her current research interests are in the field of multimodal medical visualization and illustrative medical visualization.

THURSDAY JUNE 14th 13.00-14.20

Abdominal and cardiac/chest imaging

Moderators Kazunori Kuroki and Anselm Schultz

8 presentations

From Gd-EOB-DTPA-enhanced liver MRI with global liver function evaluation to segmental liver function assessment

Nils Dahlstrøm, Linkøping, Sweden

Introduction: Hepatobiliary MRI with Gd-EOB-DTPA is increasingly used for detection and mapping of colorectal metastases and HCC. Multi-phasic contrast-enhanced MDCT is a robust technique that gives high-quality anatomical maps of the liver vasculature as well as the liver parenchyma. There exist several CT-based dedicated semi-automatic segmentation software applications for total liver volume segmentation, separate liver segment volume measurement, liver resection simulation and liver remnant volume estimation.
For MRI datasets, however, there is a lack of similar applications. Also, there is a potential to assess liver function with MRI.

Purpose: To combine quantitative analysis of hepatocytic Gd-EOB-DTPA uptake, liver volume estimation and liver segment delineation in order to explore segmental liver function assessment based on the same Gd-EOB-DTPA-enhanced MRI of the liver, preferably with little user interaction. Connected to this procedure, we have an interest in evaluating total liver volume estimation methods and segmentation tools.

Material and method: As a measure of ”liver function”, a whole-body pharmacokinetic model of Gd-EOB-DTPA distribution and elimination was applied to Liver MRI exams on prospectively recruited patients with early-stage liver disease who were scheduled for liver biopsy. The hepatobiliary (>20 min post-injection) image series was used to measure the total liver volume, by means of manual, semi-automatic and automatic segmentation software. In a separate session, an in-house developed software for semi-automatic liver segment delineation (according to Couinaud) was used to obtain separate liver segment volumes, and to allow segmental function estimates.

Results: Using liver fibrosis as a marker of liver impairment, global liver function represented by the uptake rate of Gd-EOB-DTPA from plasma to the hepatocytes (k_{ph}) decreased in patients with advanced fibrosis. In assessing the total liver volume, there was good correlation between semi- and fully automatic segmentation software (ICC 0.9; 0.823-0.943 95% confidence interval) and the task required a mean of 5 minutes (range 1 – 18 min) compared to 60 minutes (26 – 84 min) when measurements were done manually. Initial results of segmental change in relaxation time R1 show differences between groups of segments (Couinaud 2/3, 4, 5/6, and 7/8).

Conclusion: The pharmacokinetic model has the potential of representing global liver function since the Gd-EOB-DTPA uptake parameter k_{ph} decreases for patients with advanced fibrosis. Differences in relaxation time R1, corresponding to Gd-EOB-DTPA concentration, between groups of liver segments suggest that liver function evaluation can be applied also on the segmental level. The liver volume measurement as well as liver segment delineation task are feasible to achieve on the same MRI liver dataset with reasonable operating times. Current work is directed at applying pharmacokinetic modeling also on the segmental level and to include analyses on a separate patient cohort where each subject has undergone multiple exams with Gd-EOB-DTPA.

MRI-ASSESSED TUMOR FREE DISTANCE TO SEROSA PREDICTS DEEP MYOMETRIAL INVASION AND POOR PROGNOSIS IN ENDOMETRIAL CANCER

Julie Andrea Dybvik, MD, Sigmund Ytre-Hauge, MD, Fasmer Kristine E, MSc, Inger J. Magnussen, MD, Jenny A. Husby, MD, PhD, Øyvind O. Salvesen, MSc, PhD, Jone Trovik, MD, Camilla Krakstad, MSc, PhD and Ingfrid S. Haldorsen, MD, PhD

Objective: Deep myometrial invasion (≥50% of the myometrial wall) is an important parameter for identification of high-risk disease and guides choice of surgical and adjuvant treatment in endometrial carcinomas. Currently endometrial carcinomas are staged according to the surgical pathologic International Federation of Gynecology and Obstetrics (FIGO) staging system. The aim of this study was to explore the diagnostic accuracy of preoperative magnetic resonance imaging (MRI) tumor measurements for prediction of the FIGO staging parameter deep myometrial invasion and for prognostication in endometrial cancer.

Methods/Materials: Preoperative pelvic MRI scans of 367 prospectively included patients with histologically confirmed endometrial carcinomas were read independently by three radiologists blinded to clinical information. The radiologists recorded imaging findings in a standardized registration form that included measurements of axial anteroposterior tumor diameter (AP-diameter), absolute depth of myometrial tumor invasion (DOI) in the region exhibiting proportionally deepest invasion and tumor free distance (TFD) from serosa. Receiver operating curves (ROC-curves) for prediction of deep myometrial invasion were plotted for the different tumor measurements and the prognostic values of these tumor measurements were analyzed using Kaplan-Meier analysis and univariable Cox proportional hazard model.

Results: MRI measured TFD yielded the highest area under the ROC-curve (AUC) for prediction of deep myometrial invasion with an AUC of 0.83 whereas DOI and AP-diameter yielded AUCs of 0.73 and 0.81, respectively. Low TFD, high DOI and large AP-diameter were all significantly associated with poor prognosis yielding hazard ratios of 0.87 ($p<0.001$), 1.18 ($p<0.001$) and 1.05 ($p<0.001$), respectively.

Conclusion: MRI-assessed tumor free distance to serosa, depth of myometrial invasion and AP tumor diameter predict deep myometrial invasion and prognosis in endometrial cancer.

Pancreatic fatty infiltration at Dixon-MRI is a marker of exocrine pancreatic insufficiency in cystic fibrosis (CF) - a comparison of pancreatic echogenicity at US and pancreatic fat content by MRI

Kavaliauskiene, Giedre (1,6), Engjom, Trond (2,3), Tjora, Erling (4,5), Wathle, Gaute (6), Erchinger, Friedemann (7,2), Lærum, Birger N. (5), Gilja, Odd H. (8,2), Frøkjær, Jens B. (9), Njølstad, Pål R. (5,4), Georg Dimcevski (2,3), Haldorsen, Ingfrid S. (2,6)

(1)Department of Radiology, Oslo University Hospital, Ullevål, (2) Department of Clinical Medicine, University of Bergen, (3) Department of Medicine, Haukeland University Hospital, (4) Pediatric Department, Haukeland University Hospital, (5) Department of Clinical Science, University of Bergen, (6) Department of Radiology. Haukeland University Hospital (7) Department of Medicine, Voss Hospital, Voss, (8) National Centre for Ultrasound in Gastroenterology, Haukeland University Hospital, Bergen, (9) Department of Radiology, Mech-Sense, Aalborg University Hospital

Purpose: Fatty infiltration of the pancreas is a dominating feature in patients with cystic fibrosis (CF) who have developed pancreatic insufficiency. Transabdominal ultrasound (US) often demonstrates hyperechoic pancreas in CF patients, a feature that may be due to various pathological mechanisms including fatty infiltration. The purpose of this study was to explore the association between pancreatic fat content assessed by Dixon- magnetic resonance imaging (MRI), pancreatic echogenicity at US and exocrine function in CF patients and healthy controls (HC).

Method and materials: Transabdominal US and MRI including Dixon series were performed in 21 patients with CF and in 13 HCs. Evaluation of pancreatic echogenicity was employed using visual analogue scale (VAS). Pancreatic fat- and water images (Dixon MRI) were used to calculate pancreatic fat-water ratios. Exocrine function was assessed by secretin-stimulated endoscopic short test and fecal elastase. Patient groups were classified according to exocrine pancreatic function.

Results: All CF patients with pancreatic insufficiency (CFI) had significantly increased pancreatic fat-water ratios (MRI) (mean values of 3.8 and 3.7 in the pancreatic head and body, respectively) and 90% (9/10) had hyperechoic pancreas (US). In the pancreatic sufficient CF patients (CFS) and in HCs 27% (3/11) and 38% (5/13) had a hyperechoic pancreas (US), respectively, whereas the pancreatic fat content (MRI) was low (mean fat/water ratios ranging from 0.04-0.08). Using cutoff for pancreatic fat-water ratio >0.25 (MRI) yielded 100% accuracy, 100% sensitivity and 100% specificity for the prediction of CFI among CF patients and visual analogue scale >2 for pancreatic echogenicity yielded 90% sensitivity, 67% specificity and 81% accuracy for the same.

Conclusion: Severe pancreatic fatty infiltration at Dixon-MRI is a characteristic pancreatic feature in CFI patients. Although hyperechoic pancreatic tissue is also almost uniformly observed in patients with CFI, it is quite commonly observed in CFS patients and HC, and should not be regarded as pathognomonic for pancreatic insufficiency or pancreatic lipomatosis.

Clinical relevance/application

Pancreatic Dixon-MRI nicely depicts pancreatic lipomatosis and in CF patients this is highly suggestive of exocrine pancreatic insufficiency.

Imaging features of adnexal torsion

Authors: Aya Yamane, Saiko Issiki, Akifumi Kitsuwa,Taro Ichikawa, Tadashi Kaneshiro
Naoko Takenoshita, Hiroyuki Tajima

Purpose:
To evaluate useful CT findings for the diagnosis of adnexal torsion.
Material and Methods:
From August 2008 to September 2017 consecutive forty-six female patients with adnexal torsion (age range 13-85 years) were retrospectively reviewed by medical records and PACS system.
Another forty-six female patients with acute abdomen who underwent CT (age range 13-96 years) were randomly selected for control group.
The imaging features about the adnexal torsion on plain or contrast-enhanced CT are the uterus deviation to the involved side, the mass-like lesion, and the whirl sign.
Two radiologists who were blinded to clinical information independently evaluated the presence or absence of these findings.
The sensitivity and specificity of each finding were calculated.
Results:
The sensitivity and specificity of each finding were 72% and 87% for uterus deviation, 87% and 98% for mass-like lesion, and 48% and 100% for whirl sign, respectively.
Conclusion:
The mass-like lesion finding is very useful for the detection of adnexal torsion because of its high sensitivity. The presence of the whirl sign markedly increases likelihood of adnexal torsion, while the absence of the mass-like lesion decreases it significantly.

High abdominal fat content and high visceral fat proportion are associated with advanced FIGO stage in endometrial cancer

Fasmer KE, Tangen I, Krakstad C, Haldorsen IHS. Haukeland University Hospital, Bergen, Norway

Purpose:

To explore visceral and subcutaneous fat volume assessed by computed tomography (CT) in relation to histological subtype and surgicopathological stage in endometrial cancer (EC) patients.

Materials and Methods:

Preoperative diagnostic CT scans of the abdomen were evaluated for abdominal fat content in 128 patients with histologically confirmed endometrial carcinomas. Axial images covering the abdomen from the upper right diaphragm to L5/S1-level were segmented for adipose tissue (-195 to -45 HU) in subcutaneous and visceral areas using the software iNtuition (TeraRecon Inc., San Mateo, CA, USA). Total (TAV), subcutaneous (SAV) and visceral (VAV) abdominal fat volumes were estimated together with the visceral fat percentage (VAV%= VAV/TAV), waist circumference (WC) and body mass index (BMI).

Statistical analyses were conducted to explore associations between the abdominal fat measures and tumour grade, staging parameters and oestrogen receptor (ER∝) - and progesterone receptor (PR) expression status (Mann Whitney U-test).

Results:

High TAV, VAV and WC were all significantly associated with advanced FIGO stage (III and IV, p≤0.006), presence of lymph node metastasis (p≤0.05) and high PR expression (p≤0.003). High VAV% was also associated with high FIGO stage (p=0.04), while high SAV was associated with low grade tumours (p=0.03) and high PR expression (p<0.001).

Conclusion:

CT-derived obesity markers allow novel characterization of abdominal fat distribution in endometrial cancer. Patients with advanced stage (FIGO stage III and IV) exhibited higher subcutaneous, visceral and total abdominal fat volumes and also higher visceral fat percentage (VAV%). These findings suggest that abdominal fat distribution patterns may be closely linked to the clinical phenotype in endometrial cancer. Furthermore, this study supports an important role of the metabolic tumour environment for endometrial cancer growth and spread.

Efficacy of Adrenal Venous Sampling in Primary Aldosteronism

Soma Kumasaka, Hiroyuki Tokue, Masaya Miyazaki, Kei Shibuya, Yuka Kumasaka, Ayako Taketomi-Takahashi, Yoshito Tsushima
Address: 3-39-15 Showa-machi, Maebashi, Gunma 371-8511, Japan

Objective: To evaluate the efficacy of adrenal venous sampling (AVS) in primary aldosteronism (PA).
Materials and Methods: Between January 2013 and January 2018, 72 patients (30 males, 42 females; mean age 54.1 years; range, 27-69) were given AVS in PA. Successful catheterization of the adrenal veins was confirmed by cortisol level more than 200 μg/dL in the adrenal vein after ACTH stimulation.
Result: The overall technical success rate for AVS was 91.7% (66/72). The discordance between CT/MRI results and AVS results was 62.1% (41/66). If only CT/MRI results had been used to determine lateralization of an adrenal abnormality, inappropriate adrenalectomy would have occurred in 26.1% of patients, inappropriate exclusion from adrenalectomy would have occurred in 63.6%, and adrenalectomy on the wrong side would have occurred in 8.7%. No major complications, including adrenal vein rupture, were observed.
Conclusion: We concluded that AVS was highly effective to select the appropriate treatment strategy in patients with PA.

Effect of the left atrial diameter on the quality image in coronary computed

tomography angiography (CCTA)

Tien Nguyen-Cong, Yoshiaki Ohyama, Ayako Taketomi-Takahashi, Huong Nguyen-Thu, Makito Sato, Hisako Sumiyoshi, Tetsuya Nakamura, Masahiko Kurabayashi, Yoshito Tsushima

Gunma University Graduate School of Medicine

Abstract

Purpose: To evaluate the correlation between left atrial (LA) diameter and imaging quality in coronary computed tomography angiography (CCTA).

Materials and Methods: Four hundred and twenty-six patients who underwent CCTA were included. The coronary artery attenuation, contrast-to-noise ratio (CNR) were measured in the proximal right coronary artery (RCA) and left main trunk (LMT). Then, the average of the mean values derived from RCA and LMT was calculated. On the transaxial image of non-contrast CT phase, the LA transverse diameter was measured as the maximum horizontal diameter of the left atrium at the level of the right inferior vein; the LA anterior-posterior diameter as the maximum diameter of the left atrium perpendicular to LA transverse diameter. The relationships of coronary attenuation, CNR with LA transverse, LA anterior-posterior diameter were assessed by Pearson's correlation or Spearman's rank correlation, and multivariate linear regression analysis.

Results and discussions: Coronary artery attenuation value was negatively correlated with LA anterior-posterior diameter ($r = -0.38$, $p < 0.001$) and LA transverse diameter ($r = -0.20$, $p < 0.001$). CNR was also negatively correlated with LA anterior-posterior diameter ($r = -0.16$, $p < 0.001$) and LA transverse diameter ($r = -0.11$, $p = 0.02$). In multivariable analysis that adjusted for age, gender, body surface area, heart rate, those relationships remained significant. These results might reflect higher dilution of the contrast material in the pulmonary circulation due to the processes of left ventricular diastolic dysfunction which presented with large LA. With the cut off value of 3.41 cm, the LA anterior-posterior diameter gave a specificity (Sp) of 72.2%, sensitivity (Se) of 65.7% and AUC of 0.73 for prediction of required coronary attenuation in images quality (>400 Hounsfield unit); and the results of the LA transverse diameter were: Sp = 81.3% and Se = 44.4%, AUC = 63.2% with the cut off value of 6.86 cm.

Conclusion: Coronary artery attenuation and CNR in CCTA decrease with larger LA diameter. The LA diameter should be considered for adjustment of contrast media injection protocol to get the optimal imaging quality in CCTA.

Improved three-dimensional CT image quality of high contrast anatomies with an ultra-high-resolution CT scanner: initial clinical experience

Haruhiko MACHIDA

- Haruhiko Machida, Kazunori Kuroki, Takuya Adachi, Wataru Yamamura, Hisae Shiga, Arisa Ohara, Kenichi Yokoyama
- Department of Radiology, Kyorin University Faculty of Medicine

Background: A state-of-the-art ultra-high-resolution CT (UHRCT) scanner (Aquilion Precision; Canon Medical Systems, Tokyo, Japan) providing 0.25 mm x 160 slice collimation and 1024^2 matrix size has become clinically available. The UHRCT scanner was introduced at our institution last year, and has ever been introduced at only 14 institutions in the world. Using this scanner, we compared image quality (IQ) of CT virtual bronchoscopy (CTVB) and volume-rendered (VR) temporal bone CT (TBCT) between superior (matrix size: 1024^2; slice thickness: 0.25 mm) and standard resolution reconstructions (matrix size: 512^2; slice thickness: 0.5 mm).

Methods and materials: We retrospectively enrolled 10 patients who underwent noncontrast chest CT and 11 patients, TBCT by UHRCT. The latter 11 patients showed normal temporal bone at least on one side. We generated CTVB for the former 10 patients (CTVB group), and, on an intact side, VR images of the ossicles for the latter 11 patients (TBCT group) with both the superior and standard resolution reconstructions. Two readers subjectively determined maximal recognizable bronchial-bifurcation-order in S^{1+2} of the left lung in the CTVB group, and graded delineation of the stapes using a 5-point scale (1: poor; 5: excellent) in the TBCT group. In both the groups, we compared the IQ between the superior and standard resolution reconstructions using Wilcoxon signed rank test.

Results: In the CTVB group, the maximal bifurcation order was significantly greater with the superior resolution reconstruction (mean, 10.1 ± 1.0) than with the standard resolution reconstruction (8.6 ± 0.8) ($p < 0.05$). In the TBCT group, the delineation of the stapes was significantly better with the superior resolution reconstruction (mean, 3.1 ± 1.2) than with the standard resolution reconstruction (1.0 ± 0.0) ($p < 0.05$).

Conclusion: This UHRCT scanner improves three-dimensional CT image quality of high contrast anatomies in CTVB and TBCT with the superior resolution reconstruction (matrix size: 1024^2; slice thickness: 0.25 mm).

THURSDAY JUNE 14th 15.00-16.00

Neuroimaging

Moderators: Gesche Neckelmann and Takaaki Hosoya

6 presentations

Magnetic resonance imaging of the neck in patients presenting symptoms of neck infection in emergency setting

Janne Nurminen[1], Jaakko Heikkinen[1], Jarno Velhonoja[2], Heikki Irjala[2], Kimmo Mattila[1], Jussi Hirvonen[1]

[1] Department of Radiology, University of Turku, Turku, Finland

[2] Department of Oto-Rhino-Laryngology, University of Turku, Turku, Finland

Patients with neck infection symptoms are not uncommon in emergency care setting. Neck infections may require rapid evaluation, because deep infections can lead to potentially fatal consequences, such as airway compromise, vascular complications, or mediastinitis. Traditionally, patients suspected for deep neck infection have been imaged using computed tomography (CT). However, the use of magnetic resonance imaging (MRI) has also increased in emergency care setting due to improved availability and image quality. MRI has superior soft tissue contrast compared to CT, which is highly valuable in neck imaging, since accurate determination of potential complications is essential in selecting the appropriate treatment method.

In the current study, we provide systematic retrospective data of 305 patients who were admitted to a tertiary emergency center and underwent 3 Tesla neck MRI study due to a suspected deep or complicated neck infection. The data was collected between April 1, 2014 and December 31, 2017 at the emergency center of Turku University Hospital, Turku, Finland.

Of the 305 patients suspected for deep neck infection and studied with MRI, 291 (95%) had radiological evidence of acute infection. Of these, 204 patients (70%) had one or more abscesses as defined by non-enhancing fluid collection surrounded by enhancing soft tissue. These results suggest good clinical sensitivity. Abscesses were most commonly (44% in total) found in peritonsillar, parapharyngeal, or carotid compartments. These abscesses were mostly originated from infected palatine tonsils. The second most common location of abscess was submandibular/sublingual region (22%), which is most likely explained by dental interventions or neglected dental care.

Life threatening complications were quite rare in our data, as only 11 patients (4%) suffered from mediastinitis or vascular complications.

The current study is the largest clinical sample published to date to systematically report MRI findings in suspected deep neck infections in emergency setting. We encourage clinicians and radiologists to develop a systematic pattern of using neck MRI also in the emergency setting.

Methodological considerations in designing olfactory fMRI studies

Georgiopoulos C., Witt T. S., Haller S., Dizdar N., Zachrisson H., Engström M, Larsson E.M.
Universitetssjukhuset Linköping, Östergötland 58185, Sweden

Introduction: Olfactory stimuli are transmitted from the olfactory bulb to the olfactory cortex and its main projections in the brain. The piriform cortex is the largest and most distinct structure within the olfactory cortex and can be divided, both anatomically and functionally, into the anterior piriform cortex and the posterior piriform cortex. The insula and the orbitofrontal cortex are two of the main olfactory projections beyond the olfactory cortex. Olfactory impairment is a common symptom of several neurodegenerative disorders, such as Parkinson's disease and Alzheimer's disease. Functional MRI (fMRI) has increasingly been employed in order to elucidate the neural basis of olfactory deterioration both in health and disease. The current literature about olfactory fMRI displays high methodological diversity in both the experimental designs and the analytical approaches, leading sometimes to controversial results [1-4]. The present study aims to establish a standard and easily reproducible fMRI design, by focusing on the implications of stimulation length and repetition time (TR).

Subjects and Methods: We have examined 22 healthy controls with olfactory fMRI. Our paradigm consists of two stimuli lengths (6 seconds and 15 seconds) randomly implemented in a series of 20 blocks, which are separated by 20 seconds long baseline (Figure 2). Natural coffee oil has been used as odor. Two different TRs have been tested: short TR (0.901 seconds) and long TR (1.34 seconds). Data acquisition has been performed at a 3T Siemens MAGNETOM Prisma. Collected data have been analyzed with task-driven general linear model (GLM), and task-free tensorial independent component analysis (TICA). **Results**: GLM analysis showed that the combination of short stimulus (6 seconds) and short TR (0.901 seconds) resulted in visually more extended activation within both posterior piriform cortices, compared to any other combination of stimulus length and TR (Figure 3). TICA revealed independent components that coincided temporally with the tested paradigm, for both TRs (Figure 4B and 4D). These independent components included both the posterior piriform cortex and the insula, bilaterally.

Discussion: Our current findings suggest that a combination of short odor stimulation and short TR is beneficial for detecting activation within both posterior piriform cortices and insula. These regions show a short, peak-like increase in signal after olfactory stimulation, followed by a prolonged decrease below baseline [5]. Therefore, short stimulation combined with short TR may lead to higher probability of detecting the peak of olfactory activation.

References:

1. Hummel T, Fliessbach K, Abele M, Okulla T, Reden J, Reichmann H, Wullner U, Haehner A (2010) Olfactory FMRI in patients with Parkinson's disease. Front Integr Neurosci 4:125. doi:10.3389/fnint.2010.00125

2. Moessnang C, Frank G, Bogdahn U, Winkler J, Greenlee MW, Klucken J (2011) Altered activation patterns within the olfactory network in Parkinson's disease. Cereb Cortex 21 (6):1246-1253. doi:10.1093/cercor/bhq202

3. Welge-Lussen A, Wattendorf E, Schwerdtfeger U, Fuhr P, Bilecen D, Hummel T, Westermann B (2009) Olfactory-induced brain activity in Parkinson's disease relates to the expression of event-related potentials: a functional magnetic resonance imaging study. Neuroscience 162 (2):537-543. doi:10.1016/j.neuroscience.2009.04.050

4. Westermann B, Wattendorf E, Schwerdtfeger U, Husner A, Fuhr P, Gratzl O, Hummel T, Bilecen D, Welge-Lussen A (2008) Functional imaging of the cerebral olfactory system in patients with Parkinson's disease. J Neurol Neurosurg Psychiatry 79 (1):19-24. doi:10.1136/jnnp.2006.113860

5. Poellinger A, Thomas R, Lio P, Lee A, Makris N, Rosen BR, Kwong KK (2001) Activation and habituation in olfaction--an fMRI study. Neuroimage 13 (4):547-560. doi:10.1006/nimg.2000.0713

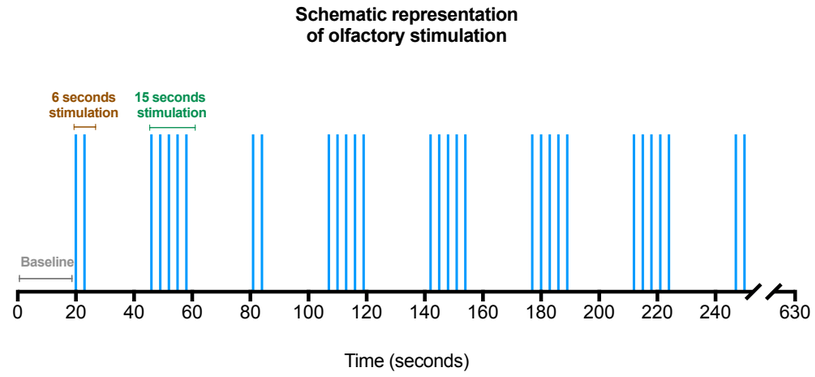

Figure 1: Schematic representation of the tested fMRI paradigm.

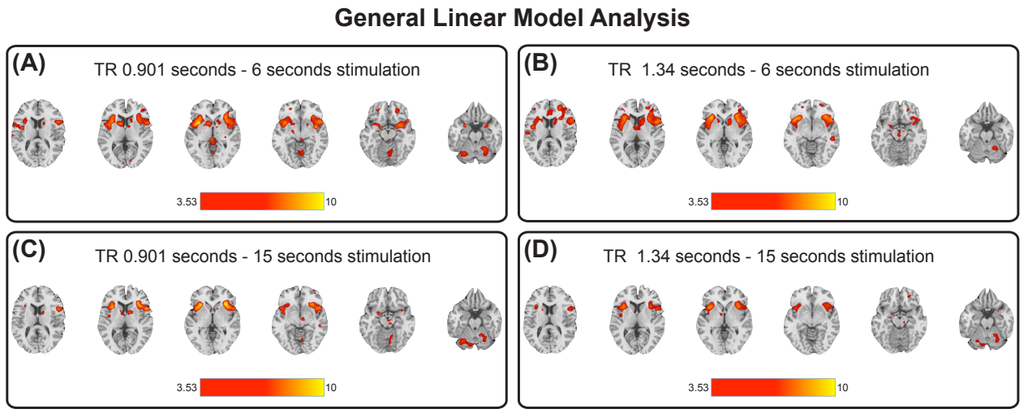

Figure 2: Main results of General Linear Model analysis

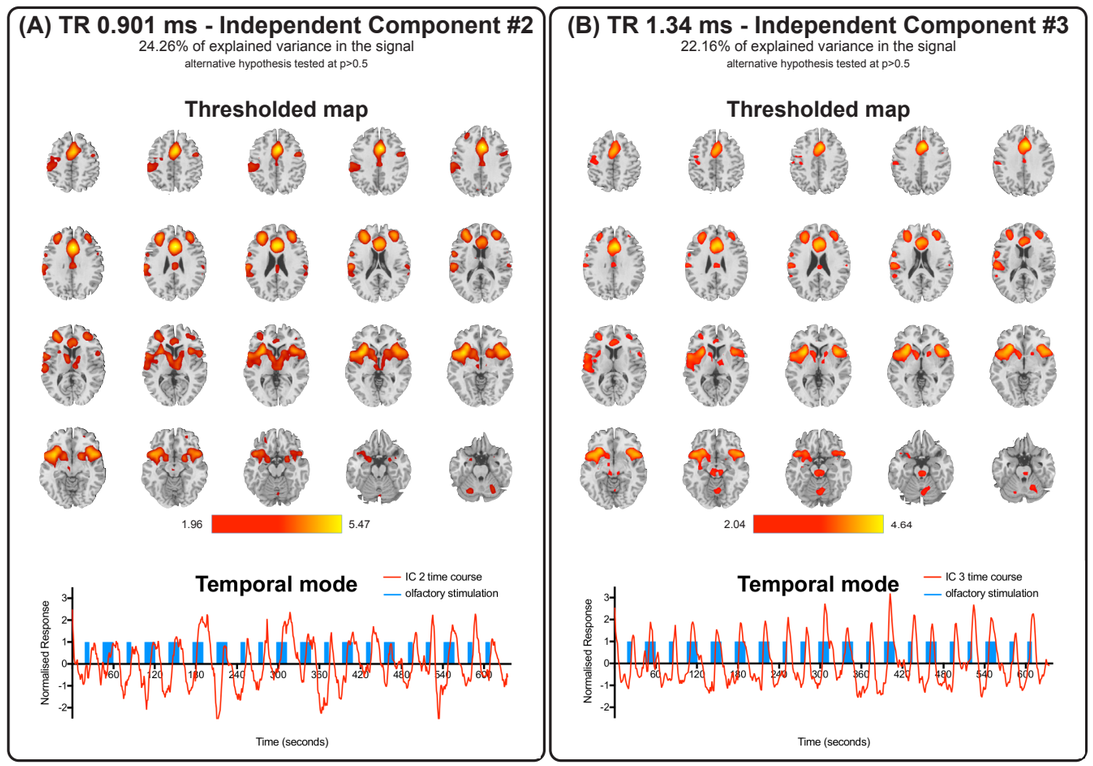

Figure 3: Main results of Tensorial Independent Component Analysis.

CT baseline findings that predict progressive paranasal sinus disease in granulomatosis with polyangiitis

Sigrun Skaar Holme[1], Karin Kilian[2], Øyvind Molberg[2], Heidi Beate Eggesbø[1]

Objectives

The purpose of this study was to identify computed tomography (CT) findings that predict development of paranasal sinus disease in patients with granulomatous polyangiitis (GPA). Secondly, we aimed to compare the ability of sequential diameter and volume measurements to evaluate the progression of sinonasal osteoneogenesis (new bone formation/bone thickening).

Methods

We retrospectively evaluated 770 CT scans in 131 GPA patients. Presence of osteoneogenesis was measured by a scoring system, and progression by the rate of change in diameters and volume. Diameter and volume rates were compared to see if the simpler diameter method performed sufficiently well. To find predictive baseline variables, we used a multivariate linear regression model with rate of change in diameters as the outcome variable.

Results

Paranasal sinus volume changes over time were appropriately measured by the diameter method. Three groups of patients were identified. One group had no osteoneogenesis, the second group had osteoneogenesis at baseline, but unchanged volume during follow-up, and the third group had progressive osteoneogenesis with decreasing volumes. Presence of severe mucosal thickening and fluid at baseline predicted progressive osteoneogenesis.

Conclusion

In patients with GPA, severe mucosal thickening and fluid at baseline CT predicted progressive osteoneogenesis. The quick and easy diameter method performed sufficiently well to measure the rates of change in paranasal sinus volume.

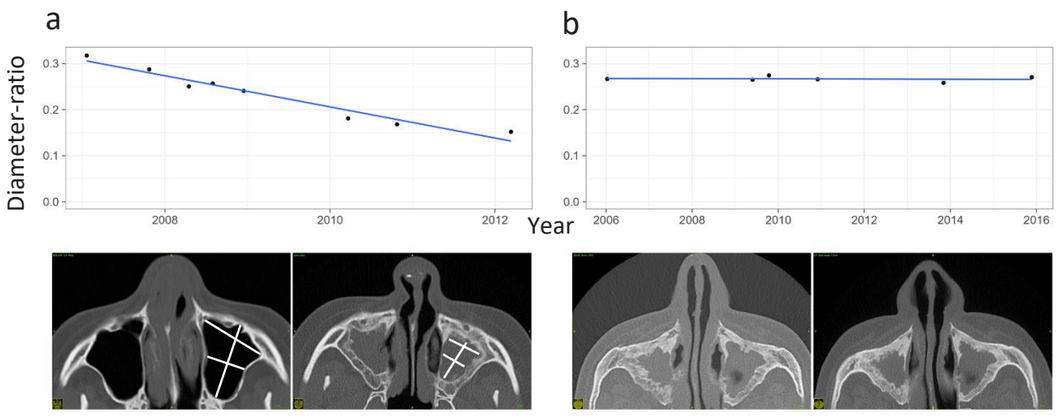

Figure 1: Progressive (a) and stable osteoneogenesis (b) in two patients. Below the graphs are pictures of the maxillary sinus from the first and last CT with the axial diameter measurements marked for patient (a).

[1] Division of Radiology and Nuclear Medicine, Oslo University Hospital
[2] Department of Rheumatology, Oslo University Hospital

Longitudinal stability of the brain functional connectome is associated with episodic memory performance.

Olga Therese Ousdal, Tobias Kaufmann, Knut Kolskår, Alexandra Vik, Eike Wehling, Astri Lundervold, Lars T Westlye, Arvid Lundervold

The brain functional connectome forms a highly individualized fingerprint that renders us distinct from one another. While much research has established that altered structural and functional brain connectivity is at the core of aging, less is known regarding the longitudinal stability of the connectome fingerprint in middle and old age. Here, we performed connectome fingerprinting on resting state functional MRI (fMRI) data acquired at two time-points separated by three years in a group of middle-aged and older adults. The results revealed that subjects could be reliably identified between the time-points, although with substantial lower identification accuracies compared to shorter time-intervals and younger subjects. Furthermore, the identification accuracies dropped with increasing age, suggesting that the individual connectivity profile is sensitive to aging processes. Notably, the longitudinal stability of the subcortical networks was associated with both cross-sectional and longitudinal measures of episodic memory performance. The findings encourage the use of connectome fingerprinting for understanding individual differences related to healthy brain aging. Furthermore, the observation that individual differences in episodic memory decline relates to the stability of subcortical networks, provide new evidence for the importance of these networks in maintaining mnemonic processing in old age.

A population study of Norwegian psychiatric patients referred for clinical brain scanning

Mona K Beyer, Turi O Dalaker, Ole Jacob Greve, Siv Elin Pignatiello, Ingrid Agartz.
Department of Radiology and Nuclear Medicine, Oslo University Hospital, Pb 4959 Nydalen, Oslo, 0424, Norway.

ABSTRACT
Objective: Patients with psychiatric conditions are often referred to a brain scan during the course of their diagnostic workup. The aim of our study is to determine frequency and type of organic brain pathology, and the relationship to age, sex and psychiatric diagnosis.
Method: We investigated MRI and CT brain scans from consecutively referred patients from the Division of Psychiatry over a 10-year period (Jan 2002-Dec 2011). The reasons for referral, estimated psychiatric diagnosis, and the pathology discovered for each patient were registered.
Results: 34% of the patients demonstrated organic brain pathology, of which 32.8% were considered clinically relevant. This represents a higher frequency of relevant pathology than reported in healthy subjects. Age ($p<0.001$) and diagnosis ($p=0.016$) were the most important determinants for frequency of pathological findings.
Conclusion: Brain imaging in clinical psychiatry resulted in around 30% positive findings, mainly due to increasing pathologies with age, but also associated with diagnosis.

Key words: Psychiatry, Pathologic findings, Magnetic Resonance Imaging, Tomography, X-Ray Computed, and Brain.

Table 1 Pathology according to psychiatric diagnosis-

Diagnosis	Number of patients	Cause of referral Routine (%)	Mean Age (SD)	Sex (M/F %)	Pathology %
Confusion/dementia	557	93	73.9 (13.2)	40/60	77. 2
Head trauma	12	100	58.2 (24.1)	50/50	66.7
Other somatic/organic disease	140	80	48.7(23.4)	52/48	44
Affective depression	390	94	53.0 (23.2)	38/62	32.3
Affective bipolar	195	95	46.1(20.6)	42/58	26.2
Anxiety (including PTSD)	19	95	36.1 (22.4)	32/68	15.8
Other	195	98	23.5 (20.0)	56/44	15.9
Psychosis	779	97	34.9 (18.8)	56/44	15.3
Substance abuse, not alcohol	16	100	28.6 (9.8)	69/31	12.5
Autism spectrum disorder, Asperger	180	99	9.3 (4.7)	81/19	7.7
Anorexia, eating disorder	14	93	16.4 (1.8)	0/100	7.1
ADHD,ADD,Tourette	187	99	13.0 (4.9)	70/30	4.3
Alcohol abuse	6	100	58.5 (5.2)	83/17	0
Whole sample	2690		43.1 (26.8)	51/49	31.8

Multi-b-value, multi-echo characterization of water diffusion within infarcted tissue

Roshan Karunamuni, San Diego, USA & Leif Oltedal, Bergen, Norway

Purpose: To determine diffusion characteristics in infarcted brain tissue by simultaneously varying the degree of diffusion weighting (b-values) and echo times (TE). **Materials and Methods:** Four patients were imaged the day after thrombectomy with standard-of-care MRI and an experimental diffusion series consisting of multiple b-values (0, 500, 1000, and 4000 s/mm^2) and multiple echo times (85.7, 103.7, and 119.4 ms). The diffusion signal decay was modeled using contributions from 4 compartments consisting of combinations of slow (0.1 um^2/ms) and fast ADC (3 um^2/ms) with short (80 ms) and long (120 ms) T2. Standard-of-care ADC maps at each echo time were also generated. **Results:** Figure 1 shows FLAIR, standard-of-care DWI and ADC and RSI-derived signal fraction (SF) volumes for one of the patients. Analysis of manually drawn regions of interest indicated a shift in SF from predominantly within the fast ADC-short T2 compartment in normal appearing tissue [mean: 0.53, sd: 0.12] to the slow ADC-long T2 compartment in infarcted tissue [mean: 0.49, sd: 0.14]. When comparing distributions of parameters in the two tissue types, t-statistics for the RSI-derived parameters ranged between 105 and 228, while those of standard-of-care ADC ranged between 57 and 64. **Conclusions**: The acquisition of diffusion weighted data with multiple echo times and multiple b-values in a single imaging series could provide clinicians

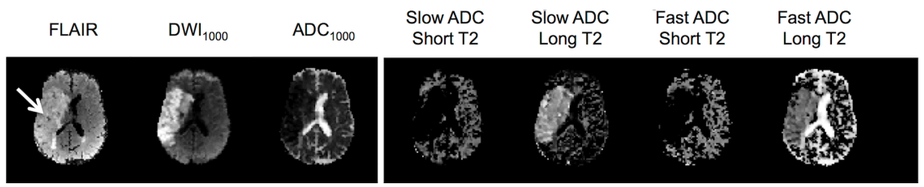

Figure 1. FLAIR, DWI-1000 (median signal at a b-value of 1000 s/mm^2, ADC: calculated using signal at b-values of 0 and 1000 s/mm^2), and SF parameter maps for one of the patients used in this study. Arrow; infarcted area.

FRIDAY JUNE 15th 08.45-09.45

Oncologic Imaging

Moderators: Rimma Axelson and Yoshio Monzen

6 presentations

Preoperative tumor texture analysis on MRI predicts high-risk disease and reduced survival in endometrial cancer

Sigmund Ytre-Hauge MD[1,2], Julie A. Dybvik MD[1], Arvid Lundervold BSc, MD, PhD[1,3], Øyvind O. Salvesen MSc, PhD[4], Camilla Krakstad PhD[5,6], Kristine E. Fasmer MSc[1,2], Henrica M. Werner MD, PhD[5,6], Balaji Ganeshan PhD[7], Erling Høivik PhD[5,6], Line Bjørge MD, PhD[5,6], Jone Trovik MD, PhD[5,6] and Ingfrid S. Haldorsen MD, PhD[1,2]

[1]Department of Radiology, Haukeland University Hospital, Bergen, Norway. [2]Section for Radiology, Department of Clinical Medicine, University of Bergen, Norway. [3]Department of Biomedicine, University of Bergen, Norway. [4]Unit for Applied Clinical Research, Department of Cancer Research and Molecular Medicine, Norwegian University of Science and Technology, Trondheim, Norway. [5]Department of Obstetrics and Gynaecology, Haukeland University Hospital, Bergen, Norway. [6]Centre for Cancer Biomarkers, Department of Clinical Science, University of Bergen, Norway. [7]Institute of Nuclear Medicine, University College London, United Kingdom.

Purpose:
To explore whether tumor texture parameters from preoperative MRI are related to known prognostic clinical and histological features (deep myometrial invasion, cervical stroma invasion, lymph node metastases and high-risk histological subtype) and to outcome in endometrial cancer patients.

Materials and Methods:
From April 2009 to November 2013 preoperative pelvic MRI (1.5T) including contrast-enhanced T1-weighted (T1c), T2-weighted (T2) and diffusion-weighted imaging (DWI) was performed in 180 patients with endometrial carcinoma, prospectively included under institutional review board approval. Tumor regions of interest (ROIs) were manually drawn on the slice displaying the largest cross-sectional tumor area, using the proprietary research software TexRAD for analysis. With filtration-histogram technique, the texture parameters standard deviation, entropy, mean of positive pixels (MPP), skewness and kurtosis were calculated. Associations between texture parameters and clinical and histological features were assessed by uni- and multivariable logistic regression, including models adjusting for preoperative biopsy status and conventional MRI findings. Multivariable Cox regression analysis was used for survival analysis.

Results:
High tumor entropy in apparent diffusion coefficient (ADC)-maps independently predicted deep myometrial invasion (OR 3.2, p<0.001), and high MPP in T1c images independently predicted high-risk histological subtype (OR 1.01, p=0.004). High kurtosis in T1c images predicted reduced recurrence- and progression-free survival (HR 1.5, p<0.001) after adjusting for MRI-measured tumor volume and histological risk at biopsy.

Conclusion:
MRI-derived tumor texture parameters independently predicted deep myometrial invasion, high-risk histological subtype and reduced survival in endometrial carcinomas, and thus, represent promising imaging biomarkers providing a more refined preoperative risk assessment that may ultimately enable better tailored treatment strategies in endometrial cancer.

ADC value negatively correlates to regional pathological grades of uterine endometrioid carcinoma

Maki Onodera, Shintaro Sugita, Yurina Onuma, Ryo Taguchi, Naoya Yama, Masamitsu Hatakenaka. S1W17 Sapporo, Hokkaido 0608556, Japan

Objectives
Endometrioid carcinoma shows a mixture of various regional differentiations in a tumor, and entire tumor grade is determined depending on the average of histology. The aim of this study was to investigate whether regional ADC values had a correlation to regional grades of endometrioid carcinoma.

Materials and methods
In this retrospective study, we evaluated 24 patients with pathologically confirmed endometrioid carcinoma who underwent preoperative MR examinations between January 2016 and March 2017, and then hysterectomy. A certified pathologist determined the regional grades depending on the rate of solid component (<=5% for G1, and >50% for G3, upgrade due to nuclear atypia) and drew the pathological maps. On the basis of the pathological maps, we measured mean ADC value of each region. **A** correlation between regional ADC values and regional grades was evaluated using Spearman rank correlation analysis.

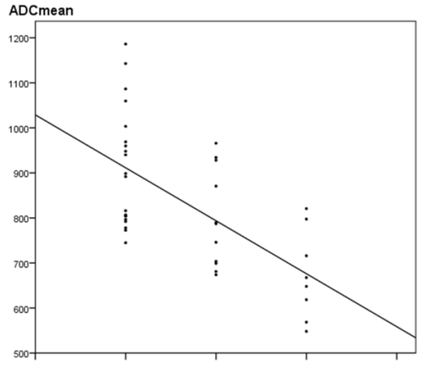

Results
The number of regional grades with the histological mapping was as follows: G1 20, G2 11, G3 8, total 39 regions. Spearman rank correlation analysis showed significant correlation between regional ADC values and regional pathological grades (r = -0.62, *P* < 0.0001, ADC value of G1=0.91±0.13x10^{-3} mm^2/sec,

Conclusion
The regional ADC values showed a significant negative correlation to regional pathological grades of endometrioid carcinoma.

ADC calculated with b-values of 0 and 1500 sec/mm2 would be superior to that with 100 and 1000 sec/mm2 in prostate cancer

Masamitsu Hatakenaka, Naoya Yama, Maki Onodera, Koichi Onodera, Naomi Koyama, Ryo Taguchi, Yurina Omura. Sapporo, Japan

Purpose

PI-RADS ver.2 recommends that DWI should include ADC map and high b-value images (b-value≥1400 sec/mm^2), and if only two b-values can be acquired, it is preferred that the lowest b-value should be set at 50-100 sec/mm^2 and the highest at 800-1000 sec/mm^2.[1] This recommendation has yet to be assured sufficiently. The present study was investigated to evaluate what combination of b-values is appropriate for calculating ADC with respect to ADC repeatability and correlation with Gleason score.

Methods

Consecutive 33 patients with histologically confirmed and DWI detectable prostate cancer (35 lesions) who underwent pelvic MRI using whole-body clinical MRI system (3T of Ingenia, Philips Medical Systems, Best, the Netherlands) to evaluate prostate in our hospital between July 2016 and December 2017 were included. All patients gave informed consent to participate in the study. Two sequential free-breathing single shot spin-echo echo-planar DWI with b-values of 0, 100, 1000 and 1500 sec/mm^2 and identical positioning were obtained during examination. The regions of interest (ROI) were assigned at 35 cancers on the 1st DWI and pasted them onto the 2nd DWI holding their size and location. Slight visual adjustment of the ROI on the 2nd DWI was performed in 5 lesions as two observers considered it is necessary to cope with minimal distortions and/or movements. Each voxel ADC was calculated by fitting signal intensity of each voxel into mono-exponential curve. ADCs calculated from several combinations of b-values were expresses as follows: ADC (0, 1000), ADC (0, 1500), ADC (100, 1000), ADC (100, 1500) and ADC (1000, 1500) were calculated with b-values of 0 and 1000 sec/mm^2, 0 and 1500 sec/mm^2, 100 and 1000 sec/mm^2, 100 and 1500 sec/mm^2 and 1000 and 1500 sec/mm^2, respectively. The repeatability of ADC histogram metrics of minimum (ADC min), 10% (ADC 10%), 25% (ADC 25%), median (ADC median), mean (ADC mean), 75% (ADC 75%), 90% (ADC 90%), maximum (ADC max), skewness (ADC skewness) and kurtosis (ADC kurtosis) of voxel-wise ADC within ROI was evaluated using intraclass correlation coefficient (ICC), Bland-Altman plot (%) and within-subject coefficient of variance (wCV%). The correlation between ADC and Gleason score was also analyzed with Spearman's rank-order correlation. $p<0.05$ was considered statistically significant.

Results

ADC skewness and kurtosis showed low repeatability irrespective of b-value combination (ICC<0.6, standard deviation of bias>300% and wCV>85%) and Spearman's rank-order correlation test was not performed for ADC skewness and kurtosis. ADC (0, 1500) showed the highest repeatability in all ADC histogram metrics except ICC of ADC min. Significant correlation with Gleason score was obtained in all ADC metrics except ADC min at least in one b-value combination. Both high repeatability and high correlation coefficient with Gleason score was observed in ADC mean and 75% calculated from ADC (0, 1500). ADC mean and 75% calculated from ADC (100, 1000) recommended by PI-RADS ver. 2 showed lower repeatability and correlation coefficient compared with those calculated from ADC (0, 1500). Details of the results were summarized in Fig. 1 and Table 1.

Conclusion

ADC calculated with b-values of 0 and 1500 sec/mm^2 is considered appropriate with respect to ADC repeatability and correlation with Gleason score when b-values of DWI were restricted to only two values due to clinical conditions.

References

1. PI-RADS Prostate Imaging - Reporting and Data System: 2015, Version 2. Weinreb JC, Barentsz JO, Choyke PL, Cornud F, Haider MA, Macura KJ, Margolis D, Schnall MD, Shtern F, Tempany CM, Thoeny HC, Verma S. Eur Urol. 2016 Jan;69(1):16-40.

Fig. 1 Bland-Altman plot of ADC 75%; ADC (100, 1000) vs. ADC (0, 1500)

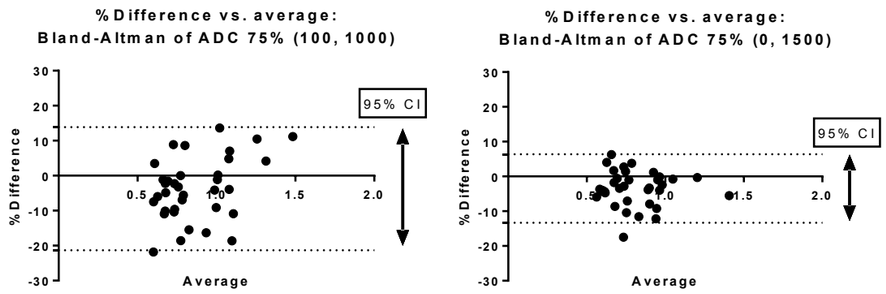

Table 1 ADC repeatability and correlation with Gleason score

ADC histogram metrics	Combination of b-values	ICC			Bland-Altman plot (%)			Within-subject coefficient of variation (wCV%)	Spearman's rank-order correlation			
			95% CI		SD of bias	95% CI			r	95% CI		p
			from	to		from	to			from	to	
ADC min	ADC (0, 1000)	0.75	0.559	0.886	35.86	-84.73	55.86	23.3				>0.05
	ADC (0, 1500)	0.731	0.529	0.854	34.56	-84.38	51.09	20.8				>0.05
	ADC (100, 1000)	0.755	0.567	0.868	198.8	-385.3	319.6	23.8				>0.05
	ADC (100, 1500)	0.607	0.347	0.78	341.2	-726.7	610.8	26.9				>0.05
	ADC (1000, 1500)	0.213	-0.13	0.506	3928	-6198	8480	251				>0.05
ADC 10%	ADC (0, 1000)	0.845	0.715	0.919	18.46	-42.97	29.41	12.2				>0.05
	ADC (0, 1500)	0.885	0.785	0.94	16.25	-37.85	25.86	9.8	-0.351	-0.619	-0.01	0.04
	ADC (100, 1000)	0.783	0.611	0.884	21.34	-47.25	36.42	14.8	-0.34	-0.611	0.003	0.05
	ADC (100, 1500)	0.796	0.633	0.892	23.82	-52.71	40.66	13.2	-0.39	-0.646	-0.055	0.02
	ADC (1000, 1500)	0.279	-0.06	0.557	450.3	-842.9	922.1	57.8				>0.05
ADC 25%	ADC (0, 1000)	0.882	0.779	0.939	13.68	-30.78	22.83	9.5	-0.355	-0.622	-0.014	0.04
	ADC (0, 1500)	0.928	0.863	0.963	10.04	-22.64	16.72	6.9	-0.388	-0.645	-0.053	0.02
	ADC (100, 1000)	0.841	0.707	0.916	15.79	-36.05	25.84	12.1	-0.348	-0.617	-0.007	0.04
	ADC (100, 1500)	0.896	0.804	0.946	11.81	-27.23	19.05	9.0	-0.409	-0.659	-0.077	0.015
	ADC (1000, 1500)	0.383	0.062	0.632	51.55	-113.9	88.2	34.8				>0.05
ADC median	ADC (0, 1000)	0.903	0.816	0.95	11.06	-24.55	18.79	8.1	-0.451	-0.687	-0.129	0.006
	ADC (0, 1500)	0.964	0.931	0.982	6.53	-16.39	9.2	5.0	-0.477	-0.704	-0.161	0.004
	ADC (100, 1000)	0.895	0.803	0.946	11.77	-27.67	18.47	9.3	-0.397	-0.651	-0.063	0.02
	ADC (100, 1500)	0.954	0.911	0.977	9.56	-23.52	13.96	6.2	-0.442	-0.681	-0.117	0.008
	ADC (1000, 1500)	0.571	0.298	0.758	30.97	-72.4	48.98	23.6	-0.455	-0.69	-0.133	0.006
ADC mean	ADC (0, 1000)	0.92	0.847	0.959	9.37	-21.64	15.08	7.1	-0.449	-0.686	-0.126	0.007
	ADC (0, 1500)	**0.969**	**0.938**	**0.984**	**6.35**	**-16.41**	**8.49**	**4.8**	**-0.498**	**-0.718**	**-0.187**	**0.002**
	ADC (100, 1000)	0.894	0.8	0.945	11.24	-26.52	17.53	8.8	-0.415	-0.663	-0.09	0.01
	ADC (100, 1500)	0.959	0.921	0.979	8.04	-20.76	10.75	5.8	-0.447	-0.685	-0.123	0.007
	ADC (1000, 1500)	0.592	0.326	0.771	28.55	-67.32	44.61	22.5	-0.472	-0.701	-0.155	0.004
ADC 75%	ADC (0, 1000)	0.93	0.866	0.964	8.34	-18.03	14.65	6.4	-0.465	-0.696	-0.145	0.005
	ADC (0, 1500)	**0.977**	**0.954**	**0.988**	**5.03**	**-13.33**	**6.39**	**4.3**	**-0.509**	**-0.725**	**-0.201**	**0.002**
	ADC (100, 1000)	0.931	0.868	0.965	8.98	-21.32	13.89	7.0	-0.444	-0.682	-0.12	0.008
	ADC (100, 1500)	0.966	0.933	0.982	6.97	-18.87	8.4	5.8	-0.483	-0.709	-0.169	0.003
	ADC (1000, 1500)	0.591	0.326	0.771	25.73	-60.7	40.17	21.0	-0.429	-0.673	-0.101	0.01
ADC 90%	ADC (0, 1000)	0.933	0.871	0.965	7.5	-16.1	13.3	5.8	-0.466	-0.697	-0.147	0.005
	ADC (0, 1500)	0.954	0.91	0.976	6.48	-16.53	8.85	5.4	-0.464	-0.696	-0.144	0.005
	ADC (100, 1000)	0.912	0.832	0.954	9.35	-21.65	14.99	7.4	-0.423	-0.669	-0.094	0.01
	ADC (100, 1500)	0.953	0.91	0.976	7.26	-19.78	8.68	6.3	-0.451	-0.687	-0.128	0.007
	ADC (1000, 1500)	0.607	0.347	0.78	22.84	-53.85	35.69	19.1	-0.471	-0.701	-0.154	0.004
ADC max	ADC (0, 1000)	0.812	0.659	0.9	12.05	-25.83	21.78	8.8				>0.05
	ADC (0, 1500)	0.897	0.805	0.946	9.39	-22.82	13.97	6.8				>0.05
	ADC (100, 1000)	0.841	0.707	0.916	12.89	-29.28	21.26	9.2				>0.05
	ADC (100, 1500)	0.869	0.757	0.932	11.53	-28.55	16.66	8.8	-0.341	-0.612	0.002	0.05
	ADC (1000, 1500)	0.508	0.214	0.717	22.41	-51.24	36.59	18.3	-0.445	-0.683	-0.122	0.007
ADC skewness	ADC (0, 1000)	0.47	0.167	0.692	300.3	-679.7	497.3	111.9				
	ADC (0, 1500)	0.398	0.079	0.643	391.5	-911.4	623.2	163.7				
	ADC (100, 1000)	0.546	0.265	0.742	383.2	-827.8	674.2	85.9				
	ADC (100, 1500)	0.445	0.135	0.675	411.2	-713.4	898.7	131.2				
	ADC (1000, 1500)	0.038	-0.3	0.362	616.2	-1196	1220	-3057.7				
ADC kurtosis	ADC (0, 1000)	0.4536	0.145	0.681	2858	-5198	6006	305.3				
	ADC (0, 1500)	0.378	0.056	0.629	2288	-5006	3964	216.0				
	ADC (100, 1000)	0.376	0.054	0.628	574.9	-948.7	1305	706.6				
	ADC (100, 1500)	0.216	-0.12	0.509	577.2	-1135	1128	230.9				
	ADC (1000, 1500)	0.1	-0.32	0.338	13085	-23165	28129	-584.2				

Can ^{18}F-FDG PET predict the response to ^{131}I radioactive iodine ablation therapy in metastatic differentiated thyroid carcinoma?

Xieyi Zhang[1], Tetsuya Higuchi[1], Arifudin Achmad[1], Anu Bhattarai[1], Hiroyasu Tomonaga[1], Huong Nguyen Thu[1], Aiko Yamaguchi[2], Hiromi Hirasawa[1], Ayako Taketomi-Takahashi[1], Yoshito Tsushima[1, 3]

[1]Department of Diagnostic Radiology and Nuclear Medicine, Gunma University, Maebashi, Japan
[2]Department of Bioimaging Information Analysis, Gunma University, Maebashi, Japan
[3]Research Program for Diagnostic and Molecular Imaging Division of Integrated Oncology Research, Gunma University Initiative for Advanced Research (GIAR), Maebashi, Japan

ABSTRACT

Purpose: To evaluate the feasibility of ^{18}F-fluorodeoxyglucose positron emission tomography (^{18}F-FDG PET) for the prediction of therapeutic response to ^{131}I radioactive iodine ablation therapy (RAI-AT) in patients with metastatic differentiated thyroid carcinoma (DTC).

Methods: We retrospectively evaluated 29 adult patients with metastatic DTC, who underwent RAI-AT after total thyroidectomy. ^{18}F-FDG PET/CT was performed within three months before RAI-AT, and the maximum, average and sum of each maximum standardized uptake value (SUV_{max}), metabolic tumor volume (MTV) and total lesion glycolysis (TLG) were assessed. Therapeutic response to RAI-AT was categorized into progressive disease (PD) or non-progressive disease (Non-PD), based on the Response Evaluation Criteria in Solid Tumor (RECIST) 1.1 using their pre- and post-therapeutic CT or MRI images. Area under curve (ROC) analyses were performed to evaluate their predictive potentials of therapeutic response to RAI-AT.

Results: Among 29 patients (12 men; median age, 62.4 y.o.; range, 26-81), eight patients were classified into PD and 21 were into Non-PD. PD patients showed a significantly higher maximum, average and sum SUV_{max}, MTV and TLG before ^{131}I therapy, compared to those of Non-PD group ($p<0.05$). Among all the PET parameters, maximum SUV_{max} showed the highest sensitivity and positive predictive value (PPV) in predicting treatment response to RAI-AT. With the cutoff value of 9.12, the highest AUC of 0.98 was obtained to differentiate between PD and Non-PD patients.

Conclusions: ^{18}F-FDG PET before RAI-AT was a useful predictor of therapeutic response to RAI-AT, and maximum SUV_{max} was the most sensitive parameter.

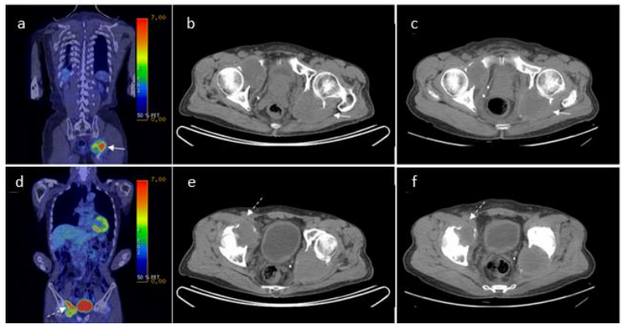

Fig. A 72-year-old male patient with pelvis metastases from left (solid arrow) and right (dash arrow) sides. The total longest diameter of pelvis metastases were decreased from 121 mm to 112 mm ten months after RAI-AT (-7.8% change defined as Non-PD). Average SUV_{max} (7.9), sum SUV_{max} (15.7), maximum MTV (183.0), average MTV (179.5), sum MTV (359.0), maximum TLG (950.4), average TLG (887.0) and sum TLG (177.4) before treatment showed an extremely high values. However, maximum SUV_{max} showed the value of 8.1 lower than the cutoff of 9.12.

a and b, pretreatment ^{18}F-FDG PET/CT of pelvis metastasis on the left side.
c, CT of pelvis metastasis on the left side acquired ten months after RAI-AT.
d and e, pre-treatment ^{18}F-FDG PET/CT scan of pelvis metastasis on the right side.
f, CT of pelvis metastasis on the right side acquired ten months after RAI-AT.

^{18}F FDG-PET/CTevaluation of histological response after neoadjuvant treatment in patients with cancer of the oesophagus or gastroesophageal junction

Gabrielson S. Sanchez-Crespo A. Klevebro F. Axelsson R. Tsai JA. Johansson O. Nilsson M.

Abstract

Background
In most parts of the world curatively intended treatment for oesophageal cancer includes neoadjuvant therapy, either with chemoradiotherapy or chemotherapy alone, followed by esophagectomy. Clinically useful tools for response evaluation are needed. Currently ^{18}F-FDG PET/CT is mainly used for preoperative disease staging, but is not well established in the evaluation of the neoadjuvant treatment.

Aims
To evaluate changes in PET parameters in relation to the histological primary tumour response in the surgical specimen in patients randomized to neoadjuvant chemoradiotherapy or chemotherapy. Study participants were all part of the NeoRes trial.

Methods
This study was part of a phase 2 trial, randomizing between neoadjuvant chemotherapy or chemoradiotherapy followed by esophagectomy.^{18}F-FDG PET/CT exams were conducted at baseline and following neoadjuvant treatment.Standardized Uptake Ratio (SUR) values were measured in the primary tumour and compared between histological responders and non-responders as well as between treatment arms.

Results
Seventy-nine patients were enrolled, and fifty-one were available for analysis. A significant rate of SUR reduction was observed (p=0.02) in the primary tumour in histological responders compared to non-responders. Changes in SUR were significantly greater in responders following chemoradiotherapy (p=0.02), but not following chemotherapy alone (p=0.49). There was a greater reduction of SUR in both response groups following chemoradiotherapy compared to chemotherapy (p=0.04).
There was no statistically significant difference in SUR in patients with a complete histological response compared to those with a subtotal response in this relatively small sample.

Conclusion
Our results are similar to those of previous studies and show that changes in the rate of SUR can be used to reliably diagnose histological responders from non-responders after neoadjuvant treatment with either chemoradiotherapy or chemotherapy.
Limitations of current PET-technology are likely to limit the possibility to accurately rule out limited residual disease.

Entropy from Preoperative CT Texture Analysis - A Potential Imaging Biomarker of Early Recurrence after Resection of Colorectal Liver Metastases

Marta Kudzmaite[1], Kristoffer Watten Brudvik[2], Karoline Skogen[1], Anne Bethke[1], Knut Jørgen Labori[2], Balaji Ganeshan[3], Johann Baptist Dormagen[1], Anselm Schulz[1]

([1]) Department of Radiology and Nuclear Medicine, Oslo University Hospital, Norway
([2]) Department of Hepato-Pancreato-Biliary Surgery, Oslo University Hospital, Norway
([3]) Institute of Nuclear Medicine, University College London, UK

Purpose: To determine the value of entropy, a CT texture analysis (CTTA) parameter, for preoperative prediction of recurrence after resection of colorectal liver metastases (CRLM).

Material and methods: Forty-four patients who underwent resection of CRLM between 2007-2009 were retrospectively included and followed-up until December 2015. CTTA was performed of the largest CRLM on contrast-enhanced CT using a research software TexRAD. Entropy was evaluated with different spatial scale filters (ssf2-6) corresponding to fine to coarse textures. A chemo-naïve group (n=41) and a chemo-exposed group (n=20) were evaluated. TexRAD identified optimal threshold-values for entropy to divide the groups into poor/good prognosis. ROC and Kaplan-Meier/multivariate Cox analyses were performed.

Results: In the chemo-naïve group, the overall time-to-recurrence was 37.3 months and the threshold-value 4.9 (filter ssf2). Below the threshold-value the overall time-to-recurrence was 46.7 months and above 21.7 months (p=0.008). Sensitivity and specificity for recurrence was 54.2% and 82.4%, respectively (p=0.447). In the chemo-exposed group, the overall time-to-recurrence was 19.2 months and the threshold-value was 4.7 (filter ssf3). Below the threshold-value the overall time-to-recurrence was 33.1 months and above 5.2 months (p=0.007). Sensitivity and specificity for recurrence was 62.5% and 100%, respectively (p=0.001).

Conclusion: Entropy derived from preoperative CTTA may have the potential to predict early recurrence, especially in patients treated with preoperative chemotherapy. In practice, this may allow improved selection for resection or focused postoperative follow-up in high-risk patients.

FRIDAY JUNE 15th 10.15-11.45

Intervention

Moderators: Hiroyuki Tajima and Mona Beyer

9 presentations

Transvenous Coil Embolization for a Dural Arteriovenous Fistula with Angiographically Isolated Transverse-Sigmoid Sinus: Multiple Microcatheter Technique via a Modern Triaxial System

Takahiko Mine, Göetz Benndorf
Depertment of Neuroradiology, Rigshospitalet, Copenhagen University Hospital, Blegdamsvej 9, 2100 København Ø, Denmark

Introduction:
Dural arteriovenous fistulas (DAVFs) involving an “isolated” transverse-sigmoid sinus (TSS) with direct cortical venous drainage (CVD) have a high risk of intracranial hemorrhage. Transvenous approach is usually not considered due to expected technical challenges to navigate catheters into the isolated sinus portion. We present a case where transvenous catheter navigation through the “occluded” sinus allowed coil embolization for DAVFs with angiographically isolated TSS using a multiple microcatheter technique via a modern triaxial system.

Case Report:
A 69-year-old woman presented pulsatile tinnitus caused by DAVFs with isolated left TSS. Via transfemoral venous approach, a triaxial system consisting of a 6Fr long sheath advanced into right jugular vein, a 6Fr intermediate catheter advanced into the angiographically patent left transverse sinus, and microcatheters was established. Two microcatheters were navigated through the thrombose segment into the isolated sinus and placed within the proximal and distal portion. Coil embolization was started with the proximal catheter to block the main draining cortical vein, and finalized with the distal catheter to block the drainage towards the deep venous system. The affected sinus segment was tightly embolized and the fistula was completely occluded. Pulsatile tinnitus disappeared immediately after the procedure.

Conclusion:
Angiography reflects the main blood stream under the local blood pressure, hence it is not always equal to actual anatomical conditions. If there are potentially patent segments despite unvisible in angiography, transvenous penetration could be less struggle and safer than transarterial liquid embolization. Multiple microcatheter approach could reduce the risk of unexpected moving of catheter tip during coil insertion and our triaxial system could provide the stable backup. Our procedure could be accomplished on the basis of the standard concept of the treatment for DAVFs and the new combination of recently advanced modalities.

C-Arm Cone-Beam CT-guided needle biopsies with prone position through the erector spinal muscle for posterior thoracic pulmonary nodules

Nobuyuki Takeyama,Toshi Hashimoto,Yoshiro Hori, Akio Kotake, Ryosuke Abe, Kazunori Kuroki, Yuki Tashiro
Address: Showa University Fujigaoka Hospital, Department of Radiology, 1-30 Fujigaoka Aoba-ku, Kanagawa Yokohama, Japan

Background: Decision of the safety entry point into the posterior thorax is a dilemma during CT-guided biopsies to prevent the intercostal artery laceration. Although it is known that an intercostal artery is shielded by the superior rib within the intercostal space in the first 6 cm lateral to the spinous process at Th7-11, this arterial position within rib space is variable according to age, cephalad rib space, and close to the spine.

Purpose: To retrospectively evaluate the technical success rate and complications of C-arm cone beam CT (CBCT)-guided needle biopsies with prone position for 64 posterior thoracic pulmonary nodules.

Material and Methods: From August 2013 to February 2018, 64 patients (mean age, 69.6 years; 48M/16F) underwent CBCT-guided biopsies with prone position through the erector spinal muscle for 64 pulmonary nodules (mean size, 32.9 mm, ranging from 7.7 to 118 mm), which were located at right apex-upper lobe (n=16), right lower lobe (n=28), left apex-upper lobe (n=4), and left lower lobe (n=16). Patients were positioned on left posterior oblique (n=16), right posterior oblique (n=26), and neutral direction (n=22). The 19/20G coaxial system was advanced through the erector spinal muscle with once puncture of the visceral pleura. Lateral distance (LD) between the puncture point of the parietal pleura and spinous process was measured on axial images. The puncture point through the parietal pleura on the intercostal space was divided into 3 areas (upper, middle, and lower areas) using sagittal images.

Results: The pathological confirmation (5 benign/58 malignancy) was obtained in 63 of 64 lesions (98.4%). The puncture point (upper, middle, and lower areas) of the intercostal space was 0,16, and 48. The averaged LD was 53.4 mm, ranging from 30 to 72 mm. Complications of hemothorax, intramuscular hemorrhage, pneumothorax, lung hemorrhage, and bloody sputum were 1, 1, 35, 28 and 4.

Conclusion: CBCT-guided needle biopsies with prone position for posterior thoracic pulmonary nodules can provide high rate of technical success with low risks of the intercostal artery laceration.

Clinical Assessment of Interventional Radiology for the Treatment of Acute Venous Thromboembolism

Center for Minimally Invasive Treatment and Department of Radiology, Nippon Medical School Musashikosugi Hospital, Kawasaki
*Department of Radiology, Nippon Medical School Hospital, Tokyo
**Department of Radiology, Teikyo University, Tokyo
Hiroyuki Tajima, Tadashi Kaneshiro, Naoko Takenoshita, Aya Yamane, Akifumi Kitsuwa, Saiko Isshiki, Taro Ichikawa, Tatsuo Ueda*, Daisuke Yasui*, Hidemasa Saito*, Izumi Tanaka*, Shiro Onozawa**, Satoru Murata**

Diagnosis and treatment for venous thromboembolic condition differs significantly depending on whether the condition is acute or chronic. The main component of treatment of acute venous thromboembolism is pharmacological anti-coagulant therapy. Systemic thrombolysis and surgical embolectomy should be considered appropriately based on the severity of the patient‘s condition.
Interventional Radiology is now available to treat most severe cases of acute massive pulmonary thromboembolism with a high mortality rate. Interventional Radiology include catheter-directed thrombolysis and catheter assisted thrombus removal. The latter is divided into aspiration thrombectomy, fragmentation, and rheolytic thrombectomy. Although no controlled clinical trials are available, data from cohort studies indicate that the clinical outcomes after surgical and catheter-tip embolectomy may be comparable.
Aggressive interventional radiology techniques for managing acute deep venous thrombosis have also evolved. Catheter directed thrombolysis was the first such procedure with demonstrated efficacy, but its acceptance has been limited by perceived risks, time to lysis, and cost. There have been some randomized controlled trial reported, there are pros and cons for this treatment. As a result, alternative measures have evolved including percutaneous other interventional procedure.
This presentation reviews the current approach to Interventional Radiology for venous thromboembolism, and shows our study with hybrid interventional treatment using a combination of local fibrinolysis, mechanical fragmentation, and clot aspiration.

Wide-necked Renal Saccular Artery Aneurysms: Long-term outcome of balloon assisted coil embolization

Tetsuhisa Yamada, Akinori Harada, Akiyoshi Yamashita
Address: Department of Radiology, Japanese Red Cross Medical Center, 4-1-22 Hiroo Shibuya-Ku, Tokyo 150-8935, Japan

Purpose:

Renal artery aneurysms (RAAs) are rare entities and their natural history remains poorly understood. Treatment is traditionally advised when aneurysm size > 20 mm, or when the patient is symptomatic or women who desire pregnancy. Endovascular treatment (EVT) is recently first line in the treatment of RAAs, however, EVT may be ineffective in excluding aneurysms with unfavorable anatomy such as wide necks or at arterial bifurcations. The aim of this paper is to report long-term outcome of balloon-assisted coil embolization for wide-necked RAAs in our institute.

Materials and Methods:

Asymptomatic 6 patients with wide-necked saccular RAAs (mean diameter 22mm: range 20-27 mm) were treated. Four was arising at the main renal arterial (mRAA) bifurcation and one was at mRAA trifurcation. The other one was arising from mRAA. 5Fr angioplasty balloon catheter was placed into the bifurcated branches across the wide-neck of RAAs. An aneurysm sac embolization was underwent using detachable coils under inflation of the balloon catheter. The follow-up was performed with three-dimensional contrast-enhanced MRA (3D-CEMRA) for evaluating after treatment of the RAAs.

Results:

The technical success rate was 100% without any complication. The followed-up periods were mean 4 years (range 1-7.4 years). Three patients showed complete occlusion with mean 26 %(range: 15-32%) decreased in size. The other three had residual flow in neck of RAAs without increasing of aneurysm size. Two of the three patients received repeat embolization due to increased neck remnants at each 1.3 year and 7 years later.

Conclusion:

Balloon assisted coil embolization is effective and safe in the treatment of wide-necked RAAs. Our methods are always possible to repeat the procedure in the event of incomplete aneurysm exclusion. Follow-up 3DCE-MRA were useful for evaluation after treatment of the RAAs

Endovascular Treatment of Type Ia Endoleak Using N-butyl Cyanoacrylate Embolization and Proximal Cuff Placement

Akio Kotake, Yoshiro Hori, Toshi Hashimoto, Norifumi Hosaka, Hiroyuki Tanaka, Susumu Takeuchi, Nobuyuki Takeyama. Address: 2-11-18-203, Azamino-minami, Aoba-ku Yokohama-city, Kanagawa 2250012, Japan

Transcatheter embolization with coils and other agents is commonly used for a type II endoleak after endovascular aortic aneurysm repair (EVAR). Standard endovascular therapy for a type Ia endoleak is a placement of aortic cuffs. There is limited published experience of a type Ia endoleak embolization.

We report a successful case of a type Ia endoleak after EVAR treated with N-butyl Cyanoacrylate (NBCA) embolization and proximal cuff placement.

Case

A 81-year-old male patient presented with a type Ia endoleak after 3 years of EVAR with Endurant II endograft for an AAA.

There was a type II endoleak from bilateral 4th lumber arteries immediately after EVAR and expectant management was chosen. A follow-up computed tomography (CT) 3 years after EVAR shows a type Ia endoleak and a contrast effect of bilateral 4th lumber arteries as a drainage route of a type Ia endoleak.

Treatment

1. Embolization of inferior mesenteric artery with coils.
2. Transcatheter Embolization with NBCA through the endoleak entry point
3. Placement of an aortic cuff

A follow-up CT at 4 months shows no evidence of an endoleak and stable aneurysm sac size.

Percutaneous intervention for tricuspid valve vegetation under intracardiac echocardiographic guidance

Daisuke Yasui, Satoru Murata, Hiroyuki Tajima, Tatsuo Ueda, Fumie Sugihara, Yasuo Miyagi, Shin-ichiro Kumita. Address: 1-1-5 Sendagi, Bunkyo-ku, Tokyo, 1138603 Japan

Pacemaker/ defibrillator lead infection is a rare but critical condition. Systemic administration of antibiotics is a standard treatment; however, removal of the infected leads are required in refractory cases. Tricuspid valve (TV) vegetation sometimes coexists, and volume reduction is required in cases of large lesion due to limited effect of antibiotics. Percutaneous intervention is often difficult since location of vegetation is unidentifiable with fluoroscopy and angiography.

This is a case series to present a novel approach: using intracardiac echocardiography (ICE) as a guide when performing percutaneous aspiration and fragmentation.

First case is a 75-year-old male with implantable cardioverter defibrillator. Signs of infection appeared 2 years later, and transesophageal echocardiography (TEE) revealed 14.6mm vegetation around right ventricular (RV) lead and 17mm vegetation in TV orifice. Manual aspiration of the vegetation was performed using 8-F guiding catheter via transfemoral approach. Both vegetation was reduced to sub-centimeter size.

The second case is a 84-year-old male with dual chamber pacemaker. Signs of infection appeared 2 years later, and transesophageal echocardiography (TEE) revealed 16.6mm vegetation around RV lead. Fragmentation was performed using coaxially inserted tri-lobe snare through 6-F aspiration catheter above and beneath TV annulus via transjugular approach, and vegetation was reduced to 6mm.

Tips of either catheter or snare was clearly visible along with vegetation using ICE in both cases.

ICE is an efficient guiding modality when performing percutaneous procedure for vegetation reduction in cases of lead infection.

Balloon-assisted transcatheter arterial n-butyl cyanoacrylate embolization of femoral artery bleeding

Tatsuo Ueda[1], Satoru Murata[2], Fumie Sugihara[1], Daisuke Yasui[1], Hidemasa Saito[1], Izumi Tanaka[1], Hiroyuki Tajima[3], Kumita S[1]
1 Department of Radiology, Nippon Medical School Hospital
2 Department of Radiology, Teikyo University Medical Center
3 Center for Minimally Invasive Treatment, Nippon Medical School Musashi-Kosugi Hospital

Purpose

To evaluate the efficacy and safety of balloon-assisted transcatheter arterial embolization (TAE) with n-butyl cyanoacrylate (NBCA) of femoral artery bleeding. Materials and Methods

The study included five patients (3 men and 2 women) with iatrogenic femoral arterial bleeding. We performed balloon-assisted TAE with NBCA which means occluded responsible bleeding artery using a balloon catheter during the embolization to prevent migration of NBCA.wT sheaths were inserted in common femoral. aArtery microcatheter was advanced into bleeding via contralateral sheath. A balloon catheter was advanced to the bleeding artery until the balloon portion covered the site of leakage via another sheath. After the balloon inflation, NBCA was slowly injected until pseudoaneurysm or extravasation was filled, but not to be attached to the balloon. The microcatheter was removed immediately after filling. We assessed overall success (complete hemostasis after the procedure) and complications.

Results

Mean age of the patients was 54.6 years. The injured arteries were common femoral artery (n = 3) and proximal site of superficial femoral artery (n = 2). We injected NBCA for two times in one case, because we could not achieve complete hemostasis in one injection. The other four cases were injected NBCA for one time. Overall success was obtained in all patients, and there were no complications including migration of NBCA. Conclusion

Balloon-assisted TAE with NBCA can be feasible, effective, and safe as a treatment of femoral artery bleeding. The potential risk of migration of NBCA could be prevented using balloon-assisted technique.

Efficacy and safety of transcatheter arterial embolization with N-butyl Cyanoacrylate for acute lower gastrointestinal bleeding

Tanaka I[1], Ueda T[1], Murata S[2], Yasui D[1], Sugihara F[1], Saito H[1], Tajima H[3], Kumita S[1].
1 Department of Radiology, Nippon Medical School
2 Department of Radiology, Teikyo University Medical Center
3 Center for Minimally Invasive Treatment, Nippon Medical School Musashi-Kosugi Hospital

Purpose:
To assess the efficacy and safety of transcatheter arterial embolization (TAE) with N-butyl Cyanoacrylate (NBCA) for acute lower gastrointestinal bleeding (LGIB).
Material and Methods:
Between June 2006 and December 2017, 62 TAE procedures with NBCA was performed in 55 patients with confirmed acute LGIB. We assessed technical success, clinical success (hemostasis in the 30 days after TAE), and bowel ischemia. TAE procedures were classified two groups as follow: group I, NBCA embolization of the within 3 vasa recta (n = 59); group II, NBCA embolization of ≥ 4 vasa recta (n=3).
Result:
Among fifty-five patients, 1 patient underwent TAE for 4 times because of multiple LGIB, and 4 patients received TAE for 2 times because of re-bleeding within 30 days after the first TAE. The other one patient underwent endoscopic treatment for re-bleeding after TAE. The procedures were successful in all patients (62 of 62 procedures), and clinical success was achieved in 92.7% (50 of 55). 5 patients with re-bleeding after TAE were all in group I. Ischemic changes were observed in 3 TAE (1 patient in group I and 2 patients in group II), and all of them required operation. Group II had higher risk of bowel ischemia than group I (p=0.0047).
Conclusion:
TAE with NBCA is an effective treatment to control acute LGIB. Although NBCA embolization of the within 3 vasa recta could be caused of re-bleeding, NBCA embolization of ≥ 4 vasa recta could induce bowel ischemia requiring operation.

Changes in aortic wall thickness related to onset of acute aortic dissection on contrast enhanced computed tomography

Hidemasa Saito, Hiromitsu Hayashi, Tatsuo Ueda, Satoru Murata, Hiroyuki Tajima, Shin-ichiro Kumita
Address: 1-1-5, Bunkyo-ku, Sendagi, Tokyo, Japan

Purpose: The aim of this study was to evaluate changes in aortic wall thickness before development of aortic dissection (AD) on contrast-enhanced computed tomography (CECT).

Materials and Methods: CECT images were retrospectively collected from 536 patients who were diagnosed with AD from October 2005 to September 2015. Of these patients, 20 patients who underwent CECT before developing AD were enrolled as an AD group. Twenty continuous patients who underwent CECT and did not develop AD were enrolled as a control group. Two radiologists manually measured wall thickness of aorta using CECT in this retrospective study. In the AD group, entry tears (ETs) were detected, and the aortic walls where the ETs caused were identified by the CECT before developing AD. The thickness of these aortic walls was defined as dissection related wall thickness (D-T). The mean wall thickness of ascending, thoracic descending, and abdominal aorta before developing AD in AD group was defined as Non dissection-related wall thickness (Non D-T). In the control group, wall thickness of aorta was measured in the same way as Non D-T, and defined as control wall thickness (C-T). We compared D-T, Non D-T, and C-T by one-way analysis of variance with Games-Howell Pairwise Comparison Test.

Results: D-T (2.20 ± 0.74 mm) was significantly thicker than both Non D-T (1.58 ± 0.22 mm) and C-T (1.56 ± 0.13 mm) (respectively, $P<0.01$).

Conclusions: Aortic walls which develop ETs of AD may be thickened.

FRIDAY JUNE 15th 13.00-13.40

PACS/informatics and education

Moderators: Finn Mathiesen and Anders Persson

4 presentations

The New European Training Assessment Programme (ETAP 2.0)

Aronen HJ, Turku, Finland

The European Training Assessment Programme (ETAP) was established in 2001 as a joint initiative between the EAR (European Association of Radiology) and the UEMS (European Union of Medical Specialists). It has been funded equally by the ESR and the UEMS. ETAP is one of the oldest collaborations between the ESR and the UEMS radiology section. The aims of ETAP are to improve and harmonize the standards of radiology training in Europe, provide institutions that offer postgraduate radiology education with objective assessment of their training programs by external assessors nominated by the ESR and UEMS and develop assessment systems and guidelines for use by postgraduate education authorities at the national level. The program has been voluntary, and visits have been made on request from the individual training centers. ETAP has also developed a self-assessment tool for training centers.

Launched in 2018, the new ETAP 2.0 has progressed from onsite assessment to virtual assessment. The assessment program is divided into the following phases: application and completion of a questionnaire, a video report of the facilities of the center, structured online interviews with the trainees, tutors and department chairperson. The final phase is certification by the Accreditation Council in Imaging (ACI). There are three levels of certification: silver, gold and platinum, based on the score reached by the center during the evaluation. A report with recommendations for improvement is sent to the center for a response within an established time frame. The evaluation is recommended to be repeated every five years.

The ETAP 2.0 program encourages self-regulation of the specialist training in radiology, further increasing the autonomy of European radiologists. The recommendations in the guidelines are compatible with the European Training Curriculum for Radiology. ETAP offers an objective method based on external systematic evaluation and self-assessment to develop radiological specialist programs in Europe and elsewhere. It is necessary that we radiologists evaluate our specialist training ourselves.

Integration of medical imaging storages using a patient-based PACS system

Takahito Nakajima, Kiyokazu Arai. Address: Kiyokazu Arai3-39-22, Showa, Maebashi, Gunma 371-8511, Japan

Background:

Patient medical imaging data are usually stored in the hospital PACS system. It is difficult to share these data among hospitals where each patient visits because there are some problems in connecting one PACS system to another hospital's PACS system, including patient ID overlapping. When patients visit another hospital, they have to bring compact discs (CDs) that contain their data. Then, each hospital imports these data into their own PACS system. In this presentation, we introduce our approach to use a cloud PACS system, which allows patients to organize and browse their own medical images, as a patient-based PACS system.

Materials and methods:

Purview ViVA (Purview; Annapolis, USA) is a cloud PACS system. For registration, patients and physicians have private IDs based on their e-mails. For image viewing, a web-based DICOM browser is used to view medical images. Data storage is in the cloud system and data are downloaded to personal computers. For data storage, an upload web page is prepared to export medical images from CDs to the cloud system. For moving data, data owners, that would be patients themselves, can transfer their data for a specific purpose to another individual by indicating a destination user ID.

Applications of this system:

- Interpretation by part time radiologists.
- Patients can manage their data in one specific storage.
- One storage for follow-up examinations
- Consultation: 1) countryside, 2) overseas, 3) among radiologists
- Second opinions for patients

Prices:

Though the pricing is not fixed, it will be similar to that of "Dropbox". Patients will pay their subscription fees monthly or annually.

Legal and ethical problems:

In this presentation, we discuss legal and ethical problems.

Plan:

We are planning to start this system in Mongolia because their country area is huge and there is a demand to consult medical images to radiologists.

PACS is coming to the era of cloud storage

Hioshi Kondah, Yonago, Japan

The EPR and PACS Sharing system of Tottori Prefecture is using a cloud technology to operate a centralized regional EPR and PACS sharing system at low cost. So we report the experiences of the latest cloud technology predicted the migration from on premises storage to cloud storage.

As the Tottori prefecture EPR and PACS sharing system could use the prefecture information highway to gather data from informant hospitals , we developed a thin client infrastructure as a countermeasure against hacking. As a response to the governmental demand, SS-MIX2 of Japan standard was introduced as the output of hospital EPR. XDS / XDS-I of IHE-ITI was introduced for an information management on center. To keep the thin client infrastructure, we gathered and stored data of EPR and PACS in the center. EPR data were gathered all the digital data, but the image data were limited to store them from one year before the patient registration because of storage volume. The images older than one year before were transferred from the PACS server of the hospital to the center by the query and retrieve command from center server. By using a large-capacity flash memory for data storage, it was faster to display images via the Internet than in the hospital network. Since the large-capacity flash memory will become less expensive than HDD. It will be popularized, so the on-premises PACS will be transformed to such a centered sharing system. Since data of a plurality of hospitals are accumulated, long-term personal data can be used and accuracy of image diagnosis can be improved. In addition, the introduction of machine learning and new analyses systems also increases. The accumulation of EPR data is also expected to improve diagnostic accuracy and improve the accuracy of analysis system including artificial intelligence.

Semiautomated segmentation of body composition in abdominal CT images using SliceOmatic – Inter- and intraobserver variation

Lisa J. Kjoenigsen, Magnus Harneshaug, Ann-Monica Floetten, Lena K. Karterud, Kent Petterson, Heidi B. Eggesboe, Peter M. Lauritzen

Introduction: Body composition segmentation of imaging examinations can provide quantitative information on distribution of tissues in the examined region. This method may for instance provide data on muscle loss (sarcopenia) or wasting (cachexia) in cancer patients, and be valuable for scientific as well as clinical purposes. Our aim was to estimate the inter- and intraobserver variation of semiautomated body composition segmentation.

Material and Methods: Anonymized, unenhanced single mid-abdominal, CT-slices were acquired from 136 patients from two previous studies. Patient informed consent and Ethics approval were obtained. CT-parameters were 120 kV, 100 or 200 mAs, with slice thickness 4 or 5 mm. Semiautomated body composition segmentation of the CT-slices was performed with the SliceOmatic software package (Tomovision) in accordance with the Alberta protocol utilizing the "region growing" function of the software. Segmentation of abdominal muscle compartment (AMC), intramuscular adipose tissue (IMAT), visceral adipose tissue (VAT) and subcutaneous adipose tissue (SAT) was performed based on the appropriate attenuation ranges for each tissue (Fig 1c).

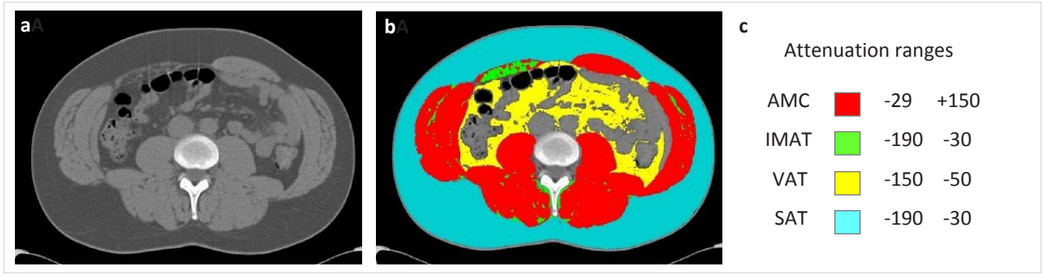

Fig 1: a) Single CT slice, b) Body composition segmentation c) Attenuation ranges.

Three radiographers and one non-radiologist physician individually performed the semiautomated segmentation.

Statistical analysis: Inter- and intraobserver variation was assessed by Intra Class Correlation (ICC) (one-way random, single measurement).

Results: Inter-and intraobserver variation measurements are summarized in the table.

Discussion: All observed ICC were > 0.9, which is considered excellent agreement. The majority of observed ICC were > 0.99, which is close to complete agreement. ICC for IMAT was slightly lower, and could be due to a more ambiguous definition of this tissue, and the relatively small area of IMAT in each slice.

Conclusion: Semiautomated body composition segmentation using SliceOmatic showed very low inter- and intraobserver variation, with close to complete agreement. This indicates a low level of operator dependability. Hence, multiple observers may interchangeably perform body composition segmentation of abdominal CT in a clinical or research setting.

Table: Inter- and intraobserver variation measurements

Value	Interobserver ICC	Reader	Intraobserver ICC
AMC	0,9967	All, combined	0,9978
		1	0,9966
		2	0,9987
		3	0,9978
IMAT	0,96	All, combined	0,9428
		1	0,9172
		2	0,9123
		3	0,9884
VAT	0,9985	All, combined	0,9987
		1	0,9992
		2	0,9977
		3	0,9997
SAT	0,9998	All, combined	0,9998
		1	0,9999
		2	0,9997
		3	0,9998

AMC: Abdominal Muscle Compartment
IMAT: Intramuscular Adipose Tissue
VAT: Visceral Adipose Tissue
SAT: Subcutaneous Adipose Tissue

FRIDAY JUNE 15th 13.40-14.40

Musculoskeletal radiology and miscellaneous

Moderators: Jenny Husby and Hiroshi Kondo

6 presentations

Extra-osseous uptake of bone scintigraphic agent DPD

Tore Bach-Gansmo

Department of Radiology and Nuclear Medicine, Oslo University Hospital, Oslo, Norway.

Abstract

Objective: DPD (^{99m}Tc-3,3-diphosphono-1,2-propanodicarboxylic acid , Teceos®) has been used intermittently for bone scintigraphy at various institutions in Norway since 2010. Extraosseous uptake, in particular, myocardial uptake, has been observed in a number of patients, and is associated with TTR-amyloidosis. Additionally, reduced quality of the bone scans and increased pulmonary uptake is apparent in many of these patients. The aim of this quality control was to assess extra cardial soft tissue uptake in the patients with high myocardial uptake.

Methods: A retrospective analysis of 2435 bone scintigraphies performed during a 3 year period revealed relatively intense myocardial uptake in 10 of the 1195 patients examined with DPD (Teceos®), close to 1% of the bone scans performed with DPD.

A comparison of pulmonary uptake in a control group of age and gender matched subjects examined during the same period was performed. Three of the 10 patients examined with DPD had several DPD and also MDP scans which allowed an intra-patient comparison.

Results: In patients with cardiac uptake of DPD, it could also be shown a relatively intense background uptake in the lungs with significantly higher uptake ratio over intercostals regions vs. the abdomen, compared to the control groups. Furthermore we found, as already well documented, a significantly lower bone to soft tissue uptake in these patients, as quantified by a femur to surrounding soft tissue ratio.

Conclusion: Cardiac uptake of bone scintigraphic agents is associated with high pulmonary uptake. This may give DPD a new role in understanding extraosseous bone tracer uptake.

Diagnosis of peri-prosthetic infection at the hip using standard uptake value of 99mTc-bone SPECT

Naoya Yama, Satoshi Nagoya, Ryo Taguchi, Naomi Koyama, Koichi Onodera, Maki Onodera, Masamitsu Hatakenaka

Address: Chuo-ku, S-1, W-16, Sapporo, Hokkaido 060-8543, Japan

<Background> Accuracy of differentiation of peri-prosthetic infection at the hip from non-infection using three phase 99mTc-bone scintigraphy is about 50-70%, and not enough[1].

<Purpose> To evaluate retrospectively whether standard uptake value (SUV) of 99mTc-bone SPECT could differentiate peri-prosthetic infection at the hip from non-infection.

<Material and method> 18 patients who were suspected peri-prosthetic infection at hip and underwent 99mTc-bone SPECT and surgical intervention with bacterial examination between April 2014 and March 2016 were included. Patients with confirmation of infection from bacterial examination allocated infection group and without allocated non-infection group. Semi-quantitative analysis was performed using maximum SUVs of 99mTc-bone SPECT, obtained from blood pool phase images (SUVmaxBP) and bone phase images (SUVmaxBN). These values were compared between infection and non-infection groups using the Mann–Whitney U test. A $P<0.05$ was considered statistically significant.

<Result> The result was shown on figure. Of 18 patients, 11 patients were allocated infection group; remaining 7 patients were allocated non-infection group. There was a significant difference in SVUmaxBN (14.42±5.58 for infection vs. 8.56±3.73 for non-infection, P=0.027) and no significance in SVUmaxBP (4.36±1.28 for infection vs. 3.77±1.08 for non-infection, P=0.43). At a cut-off SVUmaxBN value of 10.00, the sensitivity, specificity and accuracy were 0.73, 0.86, and 0.78.

<Conclusion> SVUmaxBN is a useful parameter to differentiate peri-prosthetic infection at the hip from non-infection and may improve the accuracy.

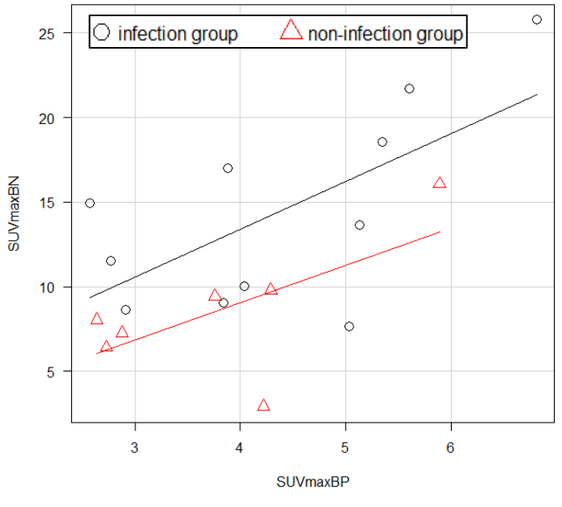

<Reference>

1) Love C et al. Nuclear medicine and the infected joint replacement. Semin Nucl Med. 39:66-78:2009

KORTUC for lytic bone metastasis

Shiro Obata,Tatsuya Takeda,Yoshiaki Ohta,Tsunehiko Kan,Shinya Kanegae, Yohta Inoue, Akira Kuroiwa,
Department of Radiology and Radiotherapy, Nagasaki Prefecture Shimabara Hospital, Shimokawajiri 7895, Shimabara, Nagasaki 855-0861, Japan

Objective: To improve the effect of irradiation for lytic bone metastasis, we added a new radio-sensitizer injection to the lesion directly under image guide (KORTUC) after our ethics committee approval. We have experienced 25 cases with patient's consent from 2010. Herein, we report clinical data retrospectively.
Materials and Method: We selected 20 eligible patients our hospital followed up. Patient age was 42-83 years, the ratio of men to women was 12: 8. As for the primary legion, lung was 12 cases, 3 rectums, 2 esophaguses, and others. Uncontrolled primary lesion was 16 cases. 16 cases accompanied other metastasis. Affected bone was 9 pelvic bones, extremities bone 5, thorax 2, and others. Performance status 3-4 was 7 cases, uncontrollable pain was recognized in 18 cases. We performed KORTUC in all cases. In half of the patients, chemotherapy, molecular targeted drug or immunotherapy was administered.
Results: Radiation dose was 8-54 Gy and the number of times of radio-sensitizer injection was 1-12 times. The palliative rate was 94%. 95% of the targets did not enlarge in size and half of the cases presented bone re-formation. The treatment took effect after 1-17 days and it continued for 7-630 days. The survival time was 30-1680 days. There was no severe adverse event. Neither univariate nor multivariate analysis of the local control recognized significant difference.
Conclusion: KORTUC for lytic bone metastasis was thought safe and effective. And a further accumulation of many cases is needed for recognition of a clinical option.

Future perspectives in quantitative forensic radiology

Anders Persson, Center for Medical Image Science and Visualization, Linköping university, Linköping university/US CMIV, Linköping, Sweden

Background: Postmortem imaging has been used for more than a century as a complement to medico-legal autopsies. The technique has also emerged as a possible alternative to compensate for the continuous decline in the number of clinical autopsies. Half a century ago the rate of clinical autopsies in Europe and the USA was around 60%, but since then, clinical autopsy rates have drastically declined, and is today less than 6%. Low autopsy rates may conceal medical malpractice, thereby preventing an important quality assurance indicator in health care. Further, low autopsy rates will decrease the reliability of the cause-of-death statistics, in turn decreasing the usefulness of this statistics for health care planning and research. If alternatives such as quantitative postmortem imaging techniques should turn out to be reliable in a situation where the autopsy rate is (too) low, these techniques could contribute to a more reliable cause-of-death diagnostic process. To this date several natural and unnatural causes of death and relevant forensic and pathological findings cannot be visualized or recognized in conventional post-mortem computed tomography (pmCT) and post-mortem MRI.

Method: In order to equal post-mortem imaging to autopsy in obtaining relevant morphological post-mortem information the post-mortem imaging approach has to be advanced to a level at which it can compete with classical autopsy and histology findings. Multi energy computed tomography (MECT) using more than two energies and quantitative post-mortem MRI approach can provide a substantial step into this direction.

The quantitative MR approach allows for characterizing and differentiating tissues and pathologies based on different relaxation parameter properties of tissues independent of body temperature. So far clinical MR quantification of organs or tissues was mainly conducted either quantifying T1 or T2 relaxation times to describe and characterize pathologic tissue alterations. However, usage of only one or two quantitative parameters to describe and characterize tissues limits the diagnostic abilities of the quantification approach significantly, since regular tissue adjacent to pathologic tissue can exhibit similar T1 or T2 relaxation times. A quantitative MR sequence has been developed at the Center of Medical image science and visualization (CMIV) in Linköping by Warntjes et al. This sequence allows for simultaneous quantification of T1 and T2 relaxation times plus proton density (PD) as third parameter. This new MR sequence with the combination of quantitative T1, T2 and PD values can differ basic pathologies such as infarction, hemorrhage, inflammation and fibrous tissue degeneration occurring in the different stages of myocardial infarction can be detected and discerned from unremarkable organ tissue. Moreover, thoracoabdominal organs and tissues such as heart, liver, kidneys, spleen, adipose tissue and muscle tissue has the potential to be characterized and differentiated. pmCT using dual-energy imaging is now a reality in our clinical practice, multi-energy is still in its early research stage. Based on new photon counting CT technique the entire scheme of source–object–detector could be revised in the future, optimizing spectrum and detector to the nature and composition of the target to be investigated.

Conclusion: New quantitative postmortem imaging technologies have the potential to increase the reliability of death statistics and may play an important role in quality assurance in health care in the future.

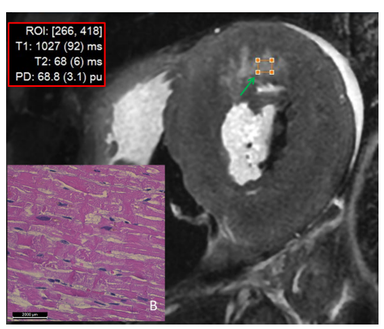

Example measurement of signal alteration in T2 weighted synthetically generated post-mortem image using SyMRI® post-processing software for PACS. A: ROIs were placed in signal alterations of sufficient size (green arrow). Quantitative T1, T2 and PD values were assessed for measured regions (red box upper left corner). In this case histologic diagnosis of early myocardial infarction was made (B).

A.Persson et al. International Journal of Legal Medicine, 2018

Incident/Accident Reports in the Radiology Department of Gunma University Hospital

Kazuhiro Kishi, RT, BS[1)], Takayuki Suto, RT, MS[1)], Hiromi Hirasawa, MD, PhD[2)]
Ayako Taketomi-Takahashi, MD, PhD, [3)], Yoshito Tsushima, MD, PhD[3)]

1)Department of Radiology, Gunma University Hospital
2)Department of General Medicine, Gunma University Hospital
3)Department of Diagnostic Radiology and Nuclear Medicine, Gunma University Graduate School of Medicine

[Purpose] Incident/accident reports are important resources for improving medical safety. Detailed evaluation of these reports can tell us the types and causes of incidents/accidents that occurred, and guide us in designing preventive measures. We evaluated the incident/accident reports made in the radiology department of our university hospital to improve not only the safety, but also the quality of medical care.
[Method] In our department, incident/accident reports are made using a specialized computer management system (Safe Master). All incident/accident reports are classified from level 0 (error made, but no incorrect procedure performed on patient), to level 5 (patient death). We retrospectively evaluated reports made over a three-year period (April 2013 to March 2016). We classified radiation technologists by experience level into less than 6 years (young), 6-15 years (middle), and 16 or more years (experienced).
[Results] A total of 393 reports were reviewed, and classified into level 0 (n=23), level 1 (n=69), level 2 (n=99), level 3a (n=144), level 3b (n=52), level 4 a(n=1), level 4 b(n=2) and level 5 (n=3). The CT section made the most reports (48.1%), followed by the conventional angiography and interventional radiology section (15.8%), X-ray section (13.2%), and radiotherapy section (9.4%). The most common incident was medication (32.1%, mainly related to contrast media), followed by therapy (excluding radiotherapy)/procedures (12.2%). 198 of 393 reports were made by nurses (50.4%), while radiation technologists made 27.5% and radiologists made 22.1%. 34 of 73 reports by the technologists (46.6%) were made by the middle group, and 26 reports (35.6%) were by the young group. Approximately 52% of the incidents/accidents were thought to be impossible to prevent in advance, i.e. first acute adverse reaction to contrast media.
[Conclusion] The incident/accident reports were mostly made in the CT section, and contrast media-related reports were the most common. More than half of were thought to be impossible to prevent in advance, but feedback of this information to medical staffs will lead to improved safety awareness, and may contribute to medical error prevention.

Evaluation of eye lens dose for percutaneous coronary intervention

Yuko Seki[1) 2)], Masashi Ando[2)], Takayuki Suto[2)], Ryuichi Funada[3)], Hiromi Hirasawa[1)], Ayako Taketomi-Takahashi[1)], Yoshito Tsushima[1)]

1) Department of Diagnostic Radiology and Nuclear Medicine, Gunma University Graduate School of Medicine
2) Department of Radiology, Gunma University Hospital
3) Department of Cardiovascular Medicine, Gunma University Hospital

Purpose: The new recommendation of the International Commission on Radiological Protection (ICRP) for the occupational eye lens dose limit is an equivalent dose limit in the eye lens of 20 mSv/year, averaged over defined 5-year periods, with no single year exceeding 50 mSv. This is far less than the previous limit of 150 mSv/year. The International Atomic Energy Agency (IAEA) recommends that equivalent eye lens dose be evaluated near the eye lens, and to evaluate the 3-mm dose equivalent. The purpose of this study was to evaluate radiation exposure to the eye lens of interventional cardiologists during percutaneous coronary intervention (PCI).
Materials and Methods: Entrance surface dose (ESD) was measured during PCI using radiophotoluminescent glass dosimeters. Doses were measured at the bilateral eye lenses (bilateral cheeks and temples within radiation protection glasses (RPGs), and left temple outside RPGs). The radioprotection effect was calculated by dividing [ESD of the left temple within RPGs] by [ESD of the left temple outside RPGs]. The effects of examination time, fluoroscopy time, air kerma, protection barriers, and the treated artery (left circumflex, left anterior descending and right coronary arteries) were also evaluated.
Results: Of the four points inside the RPGs, ESD of the left cheek had the highest radiation exposure (145.2±19.1 μGy/examination). Based on this value, the 20 mSv/year limit would be exceeded at about 140 procedures. ESD of the left cheek within RPGs linearly correlated with that outside RPGs at the left temple ($r = 0.969$, $p < 0.05$), and the radioprotection effect of RPGs was 50%. The treated artery significantly affected ESD ($p < 0.05$), and the treatment of the right coronary artery showed the highest ESD. The use of protection barriers did not significantly change ESD, and other factors also had only a weak correlation with ESD ($r = 0.024$-0.448).
Conclusion: Interventional cardiologists can potentially exceed the new lens dose limit of 20 mSv/year at approximately 140 examinations. RPGs were clearly useful for protection, but protection barriers were not.

FRIDAY JUNE 15th 15.00-15.40

Nuclear Medicine

Moderators: Hannu Aronen and Tore Bach-Gansmo

4 presentations

^{68}Ga-PSMA PET/CT- a magic bullet?

Initial experience from Karolinska University hospital, Huddinge, Sweden

Rimma Axelsson

Address: Karolinska University Hospital, Huddinge, Sweden

In 2015, there were 10 436 new diagnosed PCa cases in Sweden. In about 90% of these patients the disease is localized to the prostate gland. Surgical removal of the prostate is considered as a curative treatment. Pre-operative staging is recommended in patients with high risk prostate cancer and the nomogram (https://www.mskcc.org/nomograms) from 2012 is used in our hospital to evaluate the individual patient's risk of lymph node engagement. Preoperative staging is a major challenge for all conventional imaging methods. Abdominal CT and MRI have similar performances in prostate cancer nodal staging with a sensitivity of below 40%. Although choline-based Positron Emission Tomography (PET)/CT is used for this purpose, there have been numerous studies reporting a low sensitivity and specificity, especially at low PSA levels and high Gleason scores. Therefore, extensive Pelvic Lymph Node Dissection (ePLND) is considered the most accurate for assessment of nodal involvement by European Association of Urology and is recommended by Swedish National Guidelines.

Fortunately metastases will only occur in about 5-15%, which means that 85-95% of these patients have been overtreated. This surgical procedure is associated with complications and side effects. According to National Cancer Register report from 2014, 20% of patients suffered urinary leakage and 65% of man of severe erectile dysfunction 1 year after surgery. Thus, in addition to the cost of an unnecessary lymph nodes dissection, costs for treatment of complications and side effects of this procedure should be taken into consideration. Therefore there is a considerable interest in developing an accurate non-invasive imaging biomarker that will accurately stage the primary disease in PCa patients.

The introduction of ^{68}Gallium-PSMA-11 (^{68}Ga-PSMA) for imaging PCa is one of the most remarkable developments in nuclear medicine in the recent years and the use of this tracer worldwide has happened in a very short span of time. This is probably due to the high prevalence of prostate cancer and the absence of a suitable PET tracer for this indication. Prostate specific membrane antigen (PSMA) is cell surface protein which is significantly over expressed in PCa cells. This tracer provides a promising target for PCa-specific imaging and therapy.

Early studies have demonstrated high accuracy of ^{68}Ga-PSMA-11 PET/CT in the detection of PCa metastases in different organs: even in small lymph nodes of only a few millimeters in size. A review published in October 2016 showed that the majority of studies report a high accuracy of ^{68}Ga PSMA-11 PET/CT for N-staging at primary diagnosis. Herlemann et al. demonstrated that the accuracy of ^{68}Ga PSMA-11 PET/CT (88%) was superior when compared to CT (77%) and could detect lymph node metastases in 12 patients, which were undetected by conventional imaging. Importantly, 40% of the lymph node metastases detected by ^{68}Ga PSMA-11 PET/CT were <5 mm in short axis diameter and thus undetectable by size criteria.

^{68}Ga PSMA-11 PET/CT was performed for whole body staging and also visualized bone and visceral metastases more accurately than conventional imaging (CT or bone scan). ^{68}Ga

PSMA-11 PET/CT was able to detect osseous metastases with a sensitivity and specificity of 99% and 88%, while a bone scan had a sensitivity and specificity of 87% and 61%, respectively While PSMA PET imaging may improve M-staging, it remains unclear if this advantage leads to beneficial changes in patient management.

Some studies demonstrate a change in management after ^{68}Ga PSMA-11 PET/CT in patients with both primary PCa and in cases of early biochemical recurrence. A study from Australia by Van Leeuwen et al. demonstrated a significant change in therapeutic management in 11/20 (55%) of patients scheduled to undergo salvage radiation therapy.

Thus, initial publications indicate that the new diagnostic method with ^{68}Ga- PSMA-11 PET/CT may influence the choice of treatment in patients with primary and recurrent PCa. The published studies, however, are not prospective, covers small heterogeneous patient cohorts, are single- institutional studies, have no focus on quality of life or the avoidance of unnecessary operations. Up to day there is a total lack of data evaluating methods impact on patient's treatment and outcome.

Introduction to opportunistic screening using 3T PET/MR

Eriko Maeda, Naoto Hayashi, Takeharu Yoshikawa, Soichiro Miki, Osamu Abe.

7-3-1 Hongo Bunkyo, Tokyo 1138655, Japan

Positron emission tomography (PET) performed with 18F-fluorodeoxyglucose (18F-FDG) depicts glucose-avid metabolism in tumors and inflammation. FDG-PET has long been performed in combination with CT, for the purpose of attenuation correction and acquisition of morphological information. However, addition of CT has several shortcomings, such as non-negligible radiation exposure and risks of overlooking lesions due to low tissue-attenuation contrast. Excessive radiation exposure becomes a particularly big problem when it is applied to screening, because opportunistic screening using PET-CT is nowadays prevalent in Japan. Recently, PET/MR was introduced to the in place of PET/CT in the screening facility in the University of Tokyo. In this presentation, we would like to introduce how the screening program is performed, summarize the prevalence of radiological findings in this screening program, and compared the prevalence between PET/CT and PET/MR.

A single comparison of diffusion-weighted whole body MRI with background body signal suppression (DWIBS) and FDG-PET/CT for the renal pelvic cancer.

Tsuyoshi Yoshida, Ayako Morita and Junichi Oomagari

Affiliations

PET Imaging Center, Koga Hospital 21, Kurume, Japan.

3-3-8 Miyanojin, Kurume 839-0801, Japan

Telephone: 81-942-38-3387 Telefax: 81-942-38-3341

Email: fab-1@jcom.home.ne.jp

Abstract

Purpose

In Japan, both diffusion-weighted whole body MRI with background body signal suppression (DWIBS) and FDG-PET/CT have been applied to some persons who are worried about to become cancer to find malignant lesions. Recently, we have detected a renal pelvic cancer case in a patient using both DWIBS and FDG-PET/CT. Here is presented the case and its clinical significance.

Methods

A 60s male patient underwent both DWIBS and FDG-PET/CT. MRI used a combination of a commercially available 1.5-T superconducting MR unit and a SENSE body coil (Intera Achieva; Philips Medical Systems, Best, the Netherlands). The injection dose of FDG was 259MBq (3.7MBq/kg body weight, [maximum 259MBq]). The whole body PET scan was started at one-hour after the injection of FDG to obtain both the transmission and emission data using a PET/CT camera (Biograph 40; Siemens Healthcare, Erlangen, Germany).

Results

He has a past history of early rectal cancer detected two years ago in our human cancer screening program using FDG-PET/CT. Laboratory data showed trivial inflammation sign. CRP was 0.32 mg/dl. Tumor markers (PSA/AFP/CEA/CA19-9/SCC/CYFRA) were all within normal limits. FDG-PET/CT showed only slight dilatation of right renal pelvis, and ultrasound did not show significant findings. In great concern with his past medical history, he also underwent DWIBS. And this study showed abnormally high signal in the right renal pelvis. He was sent to a urological surgeon immediately and got a diagnosis of right renal pelvic cancer. He underwent righ nephrectomy successfully. Pathological diagnosis and postsurgical staging were urothelial carcinoma, G2, pTa.

Conclusions

We could make a diagnosis of renal pelvic tumor based solely on DWIBS. This modality seems to show a better performance than FDG-PET/CT for the detectability of renal pelvic cancer.

Analysis of GBCAs Deposition Mechanism by HPLC tandem ICP-MS in Mice Following Single Dose Administration

Putri Andriana[1], A. Adhipatria P. Kartamihardja[1], Hirofumi Hanaoka[2], Satomi Kameo[3], Hiroshi Koyama[3], Ayako Takahashi-Taketomi[1], Yoshito Tsushima[1,4]

[1]Department of Diagnostic Radiology and Nuclear Medicine, Gunma University Graduate School of Medicine, Japan

[2]Department of Bioimaging Information Analysis, Gunma University Graduate School of Medicine, Japan

[3]Department of Public Health, Gunma University Graduate School of Medicine, Japan

[4]Research Program for Diagnostic and Molecular Imaging Division of Integrated Oncology Research, Gunma University Initiative for Advanced Research (GIAR), Maebashi, Japan

ABSTRACT

Objective: Recent studies have shown that gadolinium (Gd) is retained in various organs but the mechanism remains unclear. The aim of this study was to investigate Gd deposition and the potential mechanism of retention in the organs.

Materials and Methods: 10 female DdY mice, 6 weeks old were injected with either a linear GBCA (Magnevist) via tail veins at 2.5 mmol/kg. Mice were sacrificed at 3hr and 72h after injection to collect the following organs; kidney, spleen, muscle, liver, skin and bone. The protein from each sample were extracted by tissue protein extraction reagent (T-PER) at 1:10 ratio, followed by compounds separation based on its molecular size using size exclusion – high performance liquid chromatography (SE-HPLC) tandem inductively coupled plasma - mass spectrometry (ICP-MS) to measure the intensity of Gd in each fraction yielded from HPLC.

Results: The highest concentration of Gd overall was found in the kidney collected at 90 minutes (16.21 μg/g), followed by liver (0.95 μg/g), bone (0.81 μg/g), spleen (0.64 μg/g), skin (0.23 μg/g) and muscle (0.21 μg/g). Meanwhile, at time point of 3 days after injection, the highest to lowest concentration of Gd are found in the kidney (1.79 μg/g), followed by liver (0.33 μg/g), spleen (0.41 μg/g), skin (0.16 μg/g), muscle (0.12 μg/g) and bone (0.08 μg/g). Gd retention is also found as The SE-HPLC chromatogram results, suggested Gd attached to other endogenous protein, then distributed into the intracellular space.

Conclusion: Our results suggest Gd might be distributed intracellularly and deposited in the organs through chemical structure changes and reactions with compounds, especially albumin.

ABSTRACTS FOR POSTERS

12 posters

Probenecid loading enhances specific uptake of ^{18}F-3-fluoro-L-α-methyltyrosine (FAMT)

Hirofumi Hanaoka[1], Aiko Yamaguchi[1], Isa Mahendra[2], Yusri-Dwi Heryanto[2], Tetsuya Higuchi[2], Yoshito Tsushima[2],
[1]Bioimaging Information Analysis, [2]Diagnostic Radiology and Nuclear Medicine, Gunma University Graduate School of Medicine, Maebashi, JAPAN

Objectives: ^{18}F-3-fluoro-L-α-methyltyrosine (^{18}F-FAMT) is one of the clinically used promising amino acid tracer. One concern regarding the diagnosis with ^{18}F-FAMT is the possibility of false negative results, because of its relatively small absolute uptake even in malignant tumors. Therefore, a strategy that could enhance tumor accumulation of ^{18}F-FAMT would be beneficial for improving the diagnostic accuracy. It was reported that an organic anion transporter inhibitor probenecid markedly delayed the blood clearance of radioiodine labelled α-methyltyrosine, resulted in increased tumor accumulation level of the tracer. In this study, we evaluate the effect of probenecid on biodistribution of ^{18}F-FAMT in mice and discuss usefulness of probenecid for improving tumor imaging capability of ^{18}F-FAMT.
Materials and Methods: ^{18}F-acetyl hypofluoride was reacted with L-α-methyltyrosine to produce ^{18}F-FAMT. For biodistribution studies, probenecid was injected intravenously (IV, 200 mg/kg), intraperitoneally (IP, 400 mg/kg), or perorally (PO, 200 mg/kg) at 5 min (IV) or 1 h (IP and PO) before ^{18}F-FAMT injection. No pre-injection were performed for the control mice. Then, 10 min, 1 h, and 3 h after injection of ^{18}F-FAMT, mice were sacrificed and the tissues of interest were dissected out and weighed. The radioactivity was measured by using a well-type gamma counter.
Results: In control group, ^{18}F-FAMT was rapidly eliminated from the blood and also gradually cleared from the pancreas, the targeted amino acid transporter (LAT1)-positive organ. The probenecid loading delayed blood clearance and increased pancreatic accumulation level of ^{18}F-FAMT regardless of administration route. At 1 h after injection, accumulation of ^{18}F-FAMT in the blood were 0.44 ± 0.09, 1.35 ± 0.14, 1.77 ± 0.19, and 1.39 ± 0.21 % ID/g in control, IV, IP, and PO group, respectively, and those in the pancreas were 2.09 ± 0.60, 10.8 ± 1.23, 13.2 ± 2.06, and 8.96 ± 2.94 % ID/g, respectively. In IP probenecid loading group, the significantly higher blood and pancreatic radioactivity level were kept even after 3 h injection of ^{18}F-FAMT in comparison with those of control group (blood: 0.51 ± 0.06 vs 0.09 ± 0.03 % ID/g, $p<0.01$, pancreas: 4.02 ± 0.86 vs 0.50 ± 0.19 % ID/g, $p<0.01$).
Conclusion: Probenecid loading delayed the blood clearance and increased the pancreatic accumulation of ^{18}F-FAMT. These findings suggest that probenecid loading has a potential to increase tumor accumulation level of ^{18}F-FAMT.

Development of a positron emission tomography (PET) imaging agent targeting macrophage mannose receptor for the early detection of venerable plaques

Aiko Yamaguchi[1], Hirofumi Hanaoka[1], Yoshito Tsushima[2]
[1]Bioimaging Information Analysis, [2]Diagnostic Radiology and Nuclear Medicine, Gunma University Graduate School of Medicine, JAPAN

Objective: A radiolabeled mannnosylated dextran derivative, $^{99m}Tc(CO)_3$-DCM20, targeting macrophage mannose receptor (MMR) was a promising candidate for the early detection of the venerable plaques. A potential drawback of $^{99m}Tc(CO)_3$-DCM20 for the imaging of tiny atherosclerotic region in the vasculature is its relatively slow blood clearance and resolution issue of single-photon imaging. Previous studies with dextran derivatives demonstrated the influence of molecular size for their blood clearance. This study aims to develop a mannnosylated dextran derivative-based positron emission tomography (PET) imaging probe with enhanced blood clearance.

Materials and Methods: DCM10, a mannosylated dextran derivative with smaller molecular size (approx. 10 kDa) was prepared according to the reported procedure. Six-week-old ddY mice were intravenously injected with $^{99m}Tc(CO)_3$-DCM10 or $^{99m}Tc(CO)_3$-DCM20. At 10, 30, 60, and 180 min after injection, tissues of interest were dissected out and weighed. The radioactivity was measured with a well-type gamma counter. For PET imaging, (NCS-MP-NODA) 2,2′-(7-(4-isothiocyanato-benzyl)-1,4,7-triazonane-1,4-diyl)diacetic acid was conjugated with DCM10 and labeled with ^{64}Cu. A nine-month-old male apolipoprotein E-deficient ($apoE^{-/-}$) mouse, a disease model of atherosclerosis, was injected with 3 MBq of ^{64}Cu-NODA-MP-DCM10. PET imaging were performed at 1, 3, 6, and 24 h injection. Ex vivo imaging was also performed after 24-h imaging.

Results: The blood radioactivity levels of $^{99m}Tc(CO)_3$-DCM10 was significantly lower than those of $^{99m}Tc(CO)_3$-DCM20 at 10 min after injection (1.47 ± 0.34 %ID/g vs 7.37 ± 1.06 %ID/g). By contrast, high accumulation levels of $^{99m}Tc(CO)_3$-DCM10 were noted in the MMR positive organs such as liver and spleen. The liver uptake of $^{99m}Tc(CO)_3$-DCM10 and $^{99m}Tc(CO)_3$-DCM20 was 37.5 ± 1.76 %ID/g and 27.4 ± 2.57 %ID/g, respectively. In the PET image of the $apoE^{-/-}$ mouse, the highest uptake of ^{64}Cu-NODA-MP-DCM10 was observed in the liver. The accumulation of ^{64}Cu-NODA-MP-DCM10 in the coronary artery region was also observed from 1 h to 6 h after injection. Although ex vivo imaging of dissected aorta at 24 h after injection did not show any significant radioactivity uptake due to the clearance of the tracer, obvious abnormality was observed in the coronary artery region.

Conclusion: Reduction of molecular size successfully reduced the blood retention of a mannosylated-dextran derivative while keeping its affinity for MMR. The PET imaging with ^{64}Cu-NODA-MP-DCM10 showed clear radioactivity uptake in the coronary artery region of an atherosclerosis model mouse. These results suggest ^{64}Cu-NODA-MP-DCM10 warrants further validation as a PET imaging agent for the detection of venerable plaques.

Is diffusion-weighted imaging alone sufficient for the detection of colorectal liver metastases?

Anselm Schulz, Anders Drolsum, Bjørn Atle Bjørnbeth, Cathrine K Johansen, Jon Erik Holtedahl, Trond Velde Bogsrud and Nils-Einar Kløw, University of Oslo, Norway

Purpose:
To evaluate the diagnostic performance of diffusion-weighted imaging (DWI) alone for preoperative detection of colorectal liver metastases (CRLM) compared to magnetic resonance imaging (MRI) including both DWI and dynamic Gd-EOB-DTPA-enhanced sequences.

Materials and Methods:
Institutional review board approval and written informed consent were obtained. Forty-four consecutive patients with histopathological confirmed colorectal cancer and suspected CRLM underwent prospectively 1.5T liver-MRI between September 2011 and January 2013. Three image-sets were provided, each of them was evaluated by two blinded radiologists in consensus. DWI-set and DWI-T2F-set included survey, diffusion-weighted sequences (b-values 0, 50, 800s/mm²), ADC-map, and biplanar T2-weighted SSH. DWI-T2F-set included additionally respiratory-triggered T2-weighted TSE SPIR. CE/DWI-set included all sequences from the DWI-sets and Gd-EOB-DTPA-enhanced sequences.

The reference standard were histopathology and follow-up.

Results:
Reference standard found 308 liver lesions, including 132 CRLM in 40/44 patients.
Sensitivity and PPV were for DWI-set 67.4% (58.7%-75.3%) and 95.7% (89.4%-98.8%), for DWI-T2F-set 68.2% (59.5%-76.0%) and 94.7% (88.1%-98.3%) and for CE/DWI-set 88.6% (82.0%-93.5%) and 84.2% (77.0%-89.8%). CE/DWI-set was significant more sensitive than DWI-set and DWI-T2F-set ($p<0.001$, McNemar). A tendency towards higher PPV for DWI-set and DWI-T2F-set compared with CE/DWI-set was found.

Conclusion:
The diagnostic performance of DWI alone was inferior compared to liver-MRI including both DWI and Gd-EOB-DTPA-enhanced sequences. Additional T2-weighted SPIR sequence did not improve sensitivity of DWI. For optimal performance, liver-MRI should be based on both DWI and Gd-EOB-DTPA-enhanced sequences.

Optimal Preoperative Examination of Colorectal Liver Metastases: Assessment of the diagnostic performance of CT, PET/CT, MRI and Intraoperative Ultrasound

Anselm Schulz, Johann Baptist Dormagen, Tore Bach-Gansmo, Knut Jørgen Labori, Ellen Viktil, Johannes Clemens Godt, Nils-Einar Kløw.
Oslo, Norway

Abstract

Metastases from colorectal cancer are often confined to the liver. Metastases are often decisive for the prognosis. Recent developments have led to an increasing number of available treatment options. Yet, only surgical resection of all colorectal liver metastases (CRLM) has the potential of long-term survival or even cure. The choice of a suitable treatment is based on imaging, which must ensure the identification of all CRLM. However, the optimal diagnostic approach has yet to be determined.

Contrast-enhanced intraoperative ultrasound (CE-IOUS) is performed as last imaging modality prior to liver resection for CRLM. The impact of CE-IOUS on the operation strategy was evaluted. CE-IOUS was compared with preoperative imaging and the planned operation strategy with the performed operation. It was evaluated which imaging modality was superior for the identification of CRLM: CT, EOB-DTPA-enhanced MRI with diffusion-weighted imaging or PET/CT. Furthermore, it was evaluated if PET/CT with respiratory gating (rgPET/CT), a novel method for the detection of CRLM, could improve the identification of CRLM. All studies included patients with resectable CRLM.

CE-IOUS changed the operation strategy in 30% of the operations and additional 31 CRLM were identified. MRI had the highest sensitivity independent from the size of the CRLM. The overall sensitivity was 68% for CT, 90% for MRI and 61% for PET/CT. For CRLM <10 mm it was 16% for CT, 74% for MRI and 9% for PET/CT. The sensitivity of standard PET/CT combined with rgPET/CT was 68% which was significantly higher than for standard PET/CT or rgPET/CT alone.

In conclusion, CE-IOUS should be performed prior to liver resection for CRLM to optimize operation strategy. MRI has the highest sensitivity for CRLM, particularly for CRLM <10 mm. PET/CT with respiratory-gating has the potential to improve the diagnostic performance of standard PET/CT for CRLM.

References

1. Schulz A, Dormagen JB, Drolsum A, Bjornbeth BA, Labori KJ, Klow NE. Impact of contrast-enhanced intraoperative ultrasound on operation strategy in case of colorectal liver metastasis. Acta Radiol. 2012;53(10):1081-7.
2. Schulz A, Godt JC, Dormagen JB, et al. Respiratory gated PET/CT of the liver: A novel method and its impact on the detection of colorectal liver metastases. Eur J Radiol. 2015;84(8):1424-31.
3. Schulz A, Viktil E, Godt JC, et al. Diagnostic performance of CT, MRI and PET/CT in patients with suspected colorectal liver metastases: the superiority of MRI. Acta Radiol. 2015.

What combination of b-values would be appropriate for ADC calculation in uterine body lesion?

Masamitsu Hatakenaka, Naoya Yama, Maki Onodera, Koichi Onodera, Naomi Koyama, Yurina Onuma, Ryo Taguchi. Department of Diagnostic Radiology, Sapporo Medical University, South 1, West 17, Chuo-ku, Sapporo, Hokkaido 060-8556, Japan

Purpose
Reliability of image-related biomarkers has been increasing recently. The present study was investigated to evaluate what combination of b-values is appropriate for calculating ADC in terms of ADC repeatability and correlation with pathological grade in uterine body lesion.

Methods
Consecutive 14 patients with histologically confirmed uterine body lesions (5 benignancy, 7 endometrioid carcinoma, 1 carcinosarcoma and 1 clear cell adenocarcinoma) who underwent pelvic MRI using whole-body clinical MRI system (1.5T or 3T of Ingenia, Philips Medical Systems, Best, the Netherlands) to evaluate pelvis in our hospital between July 2017 and January 2018 were included. All patients gave informed consent to participate in the study. Two sequential free-breathing single shot spin-echo echo-planar DWI with b-values of 0, 100, 1000 and 1500 sec/mm^2 and identical positioning were obtained during examination. The regions of interest (ROI) were assigned at endometrial lesions on the 1st DWI and pasted them onto the 2nd DWI holding their size and location. Each voxel ADC was calculated by fitting signal intensity of each voxel into mono-exponential curve. ADCs calculated from several combinations of b-values were expresses as follows: ADC (0, 1000), ADC (0, 1500), ADC (100, 1000), ADC (100, 1500) and ADC (1000, 1500) were calculated with b-values of 0 and 1000 sec/mm^2, 0 and 1500 sec/mm^2, 100 and 1000 sec/mm^2, 100 and 1500 sec/mm^2 and 1000 and 1500 sec/mm^2, respectively. The repeatability of ADC histogram metrics of minimum (ADC min), 10% (ADC 10%), 25% (ADC 25%), median (ADC median), mean (ADC mean), 75% (ADC 75%), 90% (ADC 90%), maximum (ADC max), skewness (ADC skewness) and kurtosis (ADC kurtosis) of voxel-wise ADC within ROI was evaluated using intraclass correlation coefficient (ICC), Bland-Altman plot (%) and within-subject coefficient of variance (wCV%). The correlation between ADC and grade score was also analyzed with Spearman's rank-order correlation. Benign lesions and carcinosarcoma were assigned as G0 and G3, respectively, and clear cell adenocarcinoma was excluded from histological assessment. $p<0.05$ was considered statistically significant.

Results
ADC skewness and kurtosis showed low repeatability irrespective of b-value combination (ICC<0.7, standard deviation of bias>100% and wCV>100%) and Spearman's rank-order correlation test was not performed for ADC skewness and kurtosis. ADC (0, 1500) showed the highest repeatability in all ADC histogram metrics except ADC min. Significant correlation with grade score was obtained in all ADC metrics except ADC max at least in one b-value combination. Both high repeatability and high correlation coefficient with grade score was observed in ADC10%, 25%, median and mean calculated from ADC (0, 1500). Details of the results were summarized in Fig. 1 and Table 1.

Conclusion
ADC calculated with b-values of 0 and 1500 sec/mm^2 is considered appropriate in terms of ADC repeatability and correlation with grade score when b-values of DWI were restricted to only two values due to clinical conditions.

Fig. 1 Bland-Altman plot of ADC 25%; ADC (0, 1000) vs. ADC (0, 1500)

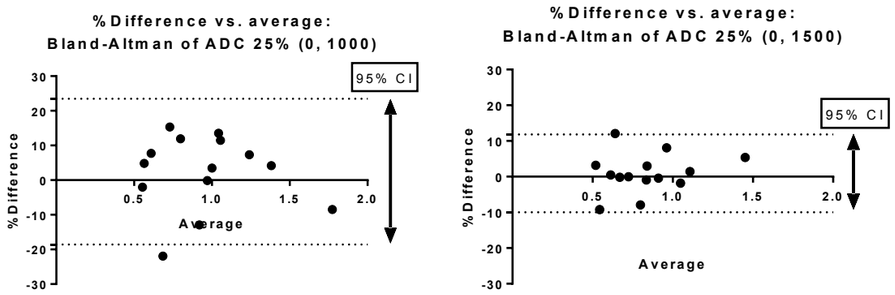

Table 1 ADC repeatability and correlation with garde score

ADC histogram metrics	Combination of b-values	ICC			Bland-Altman plot (%)			Within-subject coefficient of variation (wCV%)	Spearman's rank-order correlation	
			95% CI		SD of bias	95% CI				
			from	to		from	to		r	p
ADC min	ADC (0, 1000)	0.926	0.785	0.975	24.63	-47.6	48.94	17.93	-0.6795	0.0131
	ADC (0, 1500)	0.901	0.72	0.967	19.54	-35.62	40.96	12.42	-0.7379	0.0054
	ADC (100, 1000)	0.955	0.865	0.985	29.14	-54.54	59.68	18.67	-0.6649	0.0158
	ADC (100, 1500)	0.923	0.777	0.975	24.29	-44.79	50.43	12.34	-0.7204	0.0073
	ADC (1000, 1500)	0.768	0.419	0.919	3224	-7321	5318			>0.05
ADC 10%	ADC (0, 1000)	0.958	0.876	0.986	11.95	-23.05	23.8	7.77	-0.7933	0.0019
	ADC (0, 1500)	0.985	0.954	0.995	5.6	-9.62	12.34	3.83	-0.8108	0.0013
	ADC (100, 1000)	0.944	0.836	0.982	17.11	-35.16	31.9	10.7	-0.7204	0.0073
	ADC (100, 1500)	0.925	0.783	0.975	14.97	-32.15	26.51	8..92	-0.7466	0.0047
	ADC (1000, 1500)	0.464	-0.07	0.79	65.57	-152.9	104.2			>0.05
ADC 25%	ADC (0, 1000)	0.96	0.881	0.987	10.73	-18.58	23.49	7.19	-0.7933	0.0019
	ADC (0, 1500)	0.985	0.955	0.995	5.56	-9.96	11.82	3.67	-0.8108	0.0013
	ADC (100, 1000)	0.939	0.822	0.98	15.93	-32.01	30.42	9.64	-0.7204	0.0073
	ADC (100, 1500)	0.922	0.776	0.974	14.18	-29.02	26.55	8.76	-0.7816	0.0025
	ADC (1000, 1500)	0.475	-0.05	0.795	31.09	-69.32	52.54			0.05
ADC median	ADC (0, 1000)	0.962	0.887	0.988	10.29	-17.94	22.38	6.59	-0.767	0.0033
	ADC (0, 1500)	0.98	0.938	0.993	5.99	-9.94	13.52	4.23	-0.802	0.0016
	ADC (100, 1000)	0.909	0.741	0.97	16.86	-34.1	32.01	10.87	-0.6854	0.0121
	ADC (100, 1500)	0.927	0.788	0.976	11.96	-22.57	24.3	8.41	-0.7466	0.0047
	ADC (1000, 1500)	0.493	-0.03	0.803	25.11	-46.87	51.55			>0.05
ADC mean	ADC (0, 1000)	0.97	0.908	0.99	9.8	-17.28	21.13	6.07	-0.7758	0.0028
	ADC (0, 1500)	0.986	0.958	0.996	5.58	-8.84	13.03	3.68	-0.7758	0.0028
	ADC (100, 1000)	0.94	0.824	0.98	14.76	-29.22	28.62	9.22	-0.6766	0.0136
	ADC (100, 1500)	0.939	0.822	0.98	11.59	-22.58	22.84	7.5	-0.7204	0.0073
	ADC (1000, 1500)	0.498	-0.02	0.806	24.93	-47.25	50.47			>0.05
ADC 75%	ADC (0, 1000)	0.964	0.893	0.988	10.13	-18.06	21.65	6.32	-0.7583	0.0038
	ADC (0, 1500)	0.983	0.948	0.995	5.73	-8.59	13.88	4.08	-0.6941	0.0107
	ADC (100, 1000)	0.93	0.797	0.977	15	-29.29	29.49	9.56	-0.6766	0.0136
	ADC (100, 1500)	0.942	0.829	0.981	10.28	-19.01	21.29	7.12	-0.6941	0.0107
	ADC (1000, 1500)	0.434	-0.1	0.775	26.79	-48.59	56.44			>0.05
ADC 90%	ADC (0, 1000)	0.972	0.914	0.991	9.83	-17.76	20.78	5.89	-0.6124	0.0294
	ADC (0, 1500)	0.984	0.952	0.995	6.48	-10.51	14.87	3.86	-0.6941	0.0107
	ADC (100, 1000)	0.932	0.801	0.978	14.86	-28.07	30.19	9.63	-0.557	0.0513
	ADC (100, 1500)	0.951	0.856	0.984	10.47	-19.41	21.62	6.74	-0.6941	0.0107
	ADC (1000, 1500)	0.57	0.079	0.838	23.8	-40.7	52.58			>0.05
ADC max	ADC (0, 1000)	0.949	0.85	0.983	10.86	-18.79	23.76			>0.05
	ADC (0, 1500)	0.971	0.911	0.99	6.54	-9.95	15.7			>0.05
	ADC (100, 1000)	0.937	0.817	0.979	14.82	-27.62	30.48			>0.05
	ADC (100, 1500)	0.941	0.827	0.981	10.91	-18.64	24.15			>0.05
	ADC (1000, 1500)	0.813	0.514	0.936	22.63	-35.55	53.15			>0.05
ADC skewness	ADC (0, 1000)	0.47	0.058	0.793	3839	-7074	7975	153.66		
	ADC (0, 1500)	0.163	-0.38	0.625	322.1	-597.7	665	257.73		
	ADC (100, 1000)	-0.021	-0.53	0.498	1423	-2434	3143	406.48		
	ADC (100, 1500)	0.154	-0.39	0.619	209.3	-421.2	399.3	140.33		
	ADC (1000, 1500)	0.618	0.153	0.859	147.3	-241.3	336.3	102.32		
ADC kurtosis	ADC (0, 1000)	0.168	-0.38	0.627	247.2	-464.4	504.4	1295.28		
	ADC (0, 1500)	0.244	-0.31	0.674	426.6	-733.9	938.3	-1299.43		
	ADC (100, 1000)	0.573	0.084	0.84	139.2	-313.1	232.5	-630.68		
	ADC (100, 1500)	0.411	-0.13	0.764	616.7	-1027	1391	-812.49		
	ADC (1000, 1500)	-0.01	-0.52	0.506	7337	-16301	12459	-1258.83		

Establishment of method for r1 evaluation of paramagnetic substances and r1 determination of dissolved oxygen

Svein Are Sirirud Vatnehol et al Oslo, Norway

Background and purpose

Oxygen, like all paramagnetic substances, has the ability to change the relaxation rate (R_1) of adjacent tissues (1). R_1 is linear dependent on the relaxitivity of the substance in question and can be expressed by the equation:

$R_1 = R_{1b} + r_1[c]$,

Were R_1 is the measured relaxation, R_{1b} is the baseline relaxation without the paramagnetic substance, r_1 is the relaxation of the substance in $mMol^{-1}s^{-1}$ and [c] is the concentration of the substance in mMol. From this equation, if baseline R_1 and r_1 is known, then a measurement of R_{1b} will allow calculations of the oxygen concentration (2, 3). Previous studies have found the r_1 of oxygen to be $2.07*10^{-4}s^{-1}*mmHg^{-1}$ in vitreous at 3T (1), $2,7*10^{-4}s^{-1}*mmHg^{-1}$ in artificial CSF at 1.5T (2). Aims of the present work were: 1) to establish a technique for determination of r_1 of a paramagnetic substance, and 2) to utilize this technique to calculate the r_1 of dissolved oxygen (DO).

Methods

10 x 250 ml glass bottles with water were placed in an anoxic chamber filled with 90% N_2, 5% H_2 and 5% CO_2 for a minimum of 72 h until all dissolved oxygen (DO) was removed from the water. Zero-DO levels were confirmed using a Thermo Orion Oxygen probe. Once zero-DO was confirmed, zero-DO water and high-DO water was mixed to achieve a range of oxygen concentrations ranging from 0-30 mg/L. Immediately after preparation 100ml of each samples were removed and oxygen levels were confirmed using Winkler Titration (3). The remaining of the solution was transferred to 10 x 100 ml VWR reagent bottles, which were used for MRI relaxation analysis.

A 3T Philips Ingenia system (Philips Medical systems, Best, The Netherlands) was used for all scanning. The glass bottles containing the sample solutions were placed in a plastic container, which was subsequently filled with sun seed oil at ambient temperature. Sun seed oil was selected as filler due to less artifacts and more reliable measurements when compared to water and air in a pilot part of the study. Temperature was measured before and after scanning using a GastroMax digital thermometer. Based on previous studies at our institution three sequences were used for R1 measurement. The sequences selected in this study was a Look Locker with 5 beat readout (LL) and two Modified Look Looker Inversion recovery (MOLLI) variations with a scheme of 5(3)3 and 10(5)5. Triggering of the images was done using a simulated EKG signal of 60 beats per minute.

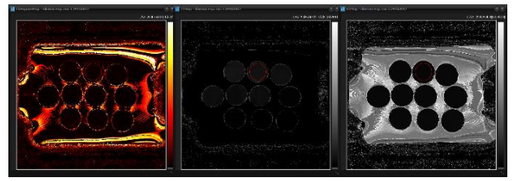

The MRI images were analysed using NoridcICE (NordicNeuroLab, Bergen, Norway) by first calculating parametric T1, R1 and Chi^2 maps. Ellipsoid ROI was drawn on the chi^2 map including as much of the fluid inside the bottle as possible, but avoiding any visible artifacts. The ROI position was then copied to the T1 and R1 maps. The T1 and R1 values were correlated with DO levels from Winkler titration in SPSS to give the degree of correlation and the r1 of DO. The experiment was repeated three times.

Figure 1. Chi^2, T1, and R1 maps of the phantom rig. An example ROI is placed in the upper-center solution (DO=1mg/L).

Results

Pearson Correlation showed significant correlation between measured R_1 and MOLLI 5(3)3 (R=0,986, p<0,001), MOLLI 10(5)5 (R=0,98, p<0,001) and Look Locker with 5 beat readout (R=0,498, p=0,013). The calculated r_1 of oxygen was found to be $4*10^{-3}$ $s^{-1}mg/L^{-1}$ for both of the MOLLI sequences and $2*10^{-3}$ $s^{-1}mg/L^{-1}$ in the LL sequence. Transforming mg/L to mmHg showed similar correlation for the MOLLI sequence but a lower correlation for LL (figure 2) and with r_1 of $2,32*10^{-4}$ $s^{-1}mmHg^{-1}$ and $2,18*10^{-3}$ $s^{-1}mmHg^{-1}$. These results are in accordance with previous published results (1, 2). There was no difference in phantom temperature between or during scanning. A total of five samples were removed from the analysis due to uncertainties in the Winkler Titration.

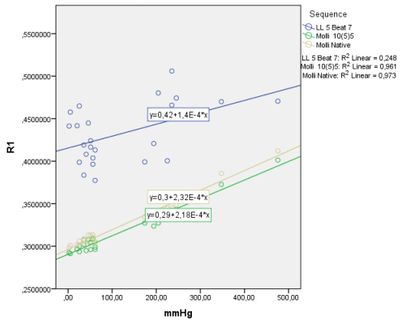

Figure 2. Scatterplots showing the correlation between R1 and mmHg for all three sequences.

Conclusions

Using two MOLLI sequences a significant correlation between R1 and levels of oxygen were found with oxygen r_1 calculated to $4*10^{-3}$ $s^{-1}mg/L$. Due to the difference in correlation, the MOLLI sequences appear more reliable than the variation of LL used in this study. The high correlation between DO and R1 indicates that this study design is suitable for r_1 determination of other dissolvable paramagnetic substances.

References

1. Muir ER, Zhang Y, San Emeterio Nateras O, Peng Q, Duong TQ. Human vitreous: MR imaging of oxygen partial pressure. Radiology. 2013;266(3):905-11.
2. Zaharchuk G, Martin AJ, Rosenthal G, Manley GT, Dillon WP. Measurement of cerebrospinal fluid oxygen partial pressure in humans using MRI. Magn Reson Med. 2005;54(1):113-21.
3. Carpenter JH. The Accuracy of the winkler method for dissolved oxygen analysis. Limnology and oceanography. 1965;10(1).

Endovenous Laser Ablation for the treatment of varicose veins in the lower extremities

Junro Hosaka, 1, 2

1 Yotsuya Vascular Clinic and 2 Department of Radiology, Nippon Medical School, Tokyo, Japan

Traditional treatment for varicose veins in the lower extremities has been Stripping operation. Usually, this method needs general anesthesia and few days of hospitalization. Scar is relatively wide and bruising and nerve disturbance after operation are problematic.
Interventional treatment for varicose veins with using laser irradiation has been developed from 2000. The principle of this method is damage of laser irradiation on venous wall, and thus, causing narrowing and thrombotic occlusion of the veins. The occluded vein will disappear in several months.
Advantages of this method are; no wide scar (it can be performed by using a catheter with 7F, maximally), no need of general anesthesia, less pain and bruising after treatment, lower rate of nerve disturbance, no radiation exposure, and no need of hospitalization.
This method brings patients of varicose veins from hospital to clinic. In these 9 years. over 6700 lower extremities have been treated in my small clinic. The results are satisfactory; rate of occluding of the veins is over 99%, rate of nerve disturbance is less than 3%, and no problematic DVT after treatment has been observed except 1 case. More details will be reported in this study.

Potential of pre-labeling method for on-site preparation of radiometal-labeled antibody

Putri Andriana[1], Hirofumi Hanaoka[2], Aiko Yamaguchi[2], Yoshito Tsushima[1]

1) Department of Diagnostic Radiology and Nuclear Medicine, Gunma University Graduate School of Medicine, Japan

2) Department of Bioimaging Information Analysis, Gunma University Graduate School of Medicine, Japan

Background/aims : Imaging with a radiolabeled antibody would be a promising strategy to select patients suitable for the respective antibody treatment. Nevertheless, widespread application of this approach is limited due to the complexity related to conventional radiolabeling technique, including requirement for time, cost, and germ free condition during chelate-antibody conjugate preparation. Pre-labeling technique, which the radiometal complex is formed first and then conjugated to the antibody, has the potential to become useful method since this technique save labor for advanced preparation of chelate-antibody conjugate. Pre-labeling technique would be more efficient and applicable for general use in clinical field, if highly-reactive and easily separable radiometal complex is available. Our aim was to develop a new bifunctional chelating agent and establish a purification method suitable for pre-labeling technique.

Methods : DO3A-PEG_2-Abz-COOH was obtained by solid phase synthesis. DO3A-PEG_2-Abz-COOH or DOTA was labeled with ^{111}In in acetate buffer or HEPES buffer. Radiochemical yield was analyzed by cellulose acetate electrophoresis. To establish a method to separate antibody from unconjugated radiometal complex, purification study was performed using a mixture of ^{111}In-DO3A-PEG_2-COOH and ^{125}I-labeled antibody. The mixture was applied to a size-exclusion cartridge, then the tracers were eluted with phosphate buffered saline, and the fractions were collected into tubes. Radioactivity of each tube was measured by γ-counter.

Result : When the standard radiolabeling condition of ^{111}In-DOTA was applied, radiochemical yield of ^{111}In-DO3A-PEG_2-Abz-COOH was approximately 91%. By using HEPES buffer instead of acetate buffer, ^{111}In-DO3A-PEG_2-Abz-COOH was obtained with radiochemical yield of more than 95%. The separation with size-exclusion cartridge yielded ^{125}I-labeled antibody with high purity with recovery yield of approximately 50% (containing less than 5% of ^{111}In-DO3A-PEG_2-Abz-COOH or ^{111}In-DOTA).

Conclusion : DO3A-PEG_4-COOH enabled ^{111}In-labeling with high radiochemical yield. The resulting radiometal complex was easily separable from antibody by using a size-exclusion cartridge. These results suggest that DO3A-PEG_2-Abz-COOH would be a promising chelate for pre-labeling technique.

Magnetic resonance imaging compatible liver phantom with 3D printed vessels

Egidijus Pelanis[1,2], Louise Oram[1], Rahul P. Kumar[1], Ole J. Elle[1,3], Bjørn Edwin[1,2]

1) The Intervention Centre, Oslo University Hospital, egidijus.pelanis@rr-research.no. 2) Institute of Clinical Medicine, Faculty of Medicine, University of Oslo, Norway. 3) Department of Informatics, University of Oslo, Oslo, Norway.

1. Background and Goal of Study

Metastatic colorectal cancer is most common in the liver and, despite advances in treatment, resection of metastasis remains the only curative option. Parenchyma-sparing laparoscopic liver resection is associated with significantly less postoperative complications for patients compared to open [1]. In some cases, this approach can be challenging, due to limited field of view and curved resection planes.

High Performance Soft-tissue Navigation (HiPerNav) is a Marie Sklodowska-Curie Actions – Innovative training network project. The consortium will address specific bottlenecks in soft tissue navigation for improved treatment of cancer.

Phantoms are needed for development and pre-clinical testing of soft-tissue navigation systems, and commercially available ones can be very expensive [2]. A simple liver phantom has been done before, although not anatomically correct [3]. A phantom can be used for laparoscopic surgical training, although to do so it needs to be anatomical correct and reasonably priced.

Therefore, development of an anatomically correct and inexpensively replaceable liver phantom is required.

2. Materials and Methods

Magnetic resonance (MR) images are segmented using tools developed through the NorMit [3] and the HiPerNav projects. Segmentations are 3D printed and used for silicon mold creation.

After initial mold creation, this liver phantom can relatively easily be reproduced as many times as needed.

3. Results and Discussion

We were able to manufacture a 0.3 scale sized, MR imaging compatible, liver phantom in less than 2 days for approximately 40 Euro, excluding the price of a 3D printer. The phantom can thereafter be reproduced for 3,15 Euro per unit.

This phantom can be designed in full scale for patient-specific planning and visualization for the surgeon, pre-surgical training and optimization of the navigation system.

4. Conclusion

A method for liver phantom manufacturing was presented and tested. A reproducible liver phantom can quickly and inexpensively be manufactured.

References

[1] Fretland, A. A., Dagenborg, V. J., Bjornelv, G. M. W., Kazaryan, A. M., Kristiansen, R., Fagerland, M. W., … Edwin, B. (2017). Laparoscopic Versus Open Resection for Colorectal Liver Metastases: The OSLO-COMET Randomized Controlled Trial. *Annals of Surgery*.

[2] Triple modality 3D abdominal phantom, Model 057A. Computerized Imaging Reference System, Inc., 2013; Accessed 3 January 2018. Available at: http://www.cirsinc.com/products/all/65/triple-modality-3d-abdominal-phantom/

[3] Langø, T., Chmarra, M. K., Hansen, R., & Ma, R. (2013). Multimodal Phantom of Liver Tissue, *8*(5), 1–9.

[4] The Norwegian center for Minimally Invasive Image Guided Therapy and medical technologies, NorMIT; Accessed 3 January 2018; Available at: http://normit.no/en

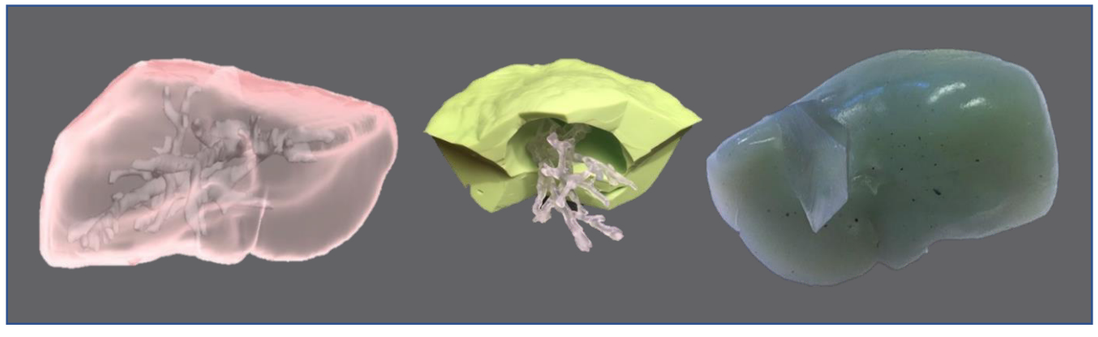

Semi-automatic liver segmentation for ground truth database development for Deep Learning Network

Pravda Jith Ray[1,2], Louise Oram[1], Ole Jakob Elle[1,2] ,Rahul Prasanna Kumar[1]

[1]The Intervention Centre, Oslo University Hospital; [2]Department of Informatics, University of Oslo

Background and Goal of study: Medical image segmentation has gained greater attention over the past few years, especially in image-guided surgery. Accurate and fast liver segmentation tools are important for liver resection planning and navigation. Currently we have developed an interactive semi-automatic method and aim to develop an automatic segmentation method, where our goal is to improve the speed and accuracy. For automatic approach we propose to use Deep Learning based methods, as recently they have shown remarkable performance in medical image analysis [1],[2].

Methods and Materials: The implementation of the semi-automatic method has been done in 3D Slicer, which is an open source software widely used by clinical practitioners and biomedical engineers for the purpose of research [3]. This segmentation work-flow starts with the user specifying the region of interest for information gathering followed by filtering using different filters. The 2D filtering process along with morphological operations followed by 3D filtering ensures an optimal segmentation results. Finally, user can make corrections for the purpose of refining the segmentation results.

Results and Discussion: The interactive approach has been applied to 10 different CT datasets and percent volume error is measured as 1.02%(obtained by comparing the volume difference after manual segmentation done with the help of an expert). This method will be evaluated in future work using larger datasets so as to validate the accuracy. The results obtained using this method will later be used as the ground truth database for the purpose of training the Deep Learning based network.

Conclusion: We have developed a semi-automatic approach with good segmentation results in CT images, which will be further evaluated on larger datasets for better validation. In the future, we will be using the results from this method for the purpose of training the Deep Learning based neural networks.

References:

[1] Litjens, G. *et al*. A survey on deep learning in medical image analysis. *arXiv preprint arXiv:1702.05747* (2017).

[2] X. Han, “Automatic liver lesion segmentation using a deep convolutional neural network method,” arXiv preprint arXiv:1704.07239, 2017.

[3] Fedorov A. et.al. “3D Slicer as an Image Computing Platform for the Quantitative Imaging Network”, *Magnetic resonance imaging*. 2012;30(9):1323-1341. doi:10.1016/j.mri.2012.05.001.

T2* of Intervertebral Discs Calculated Based on Ultra-short TE Imaging May be Promising to Evaluate Lumbar Spinal Instability

Hiroyuki Takashima, Mitsunori Yoshimoto, Rui Imamura, Noriyuki Iesato, Mitsuhiro Nakanishi, Toshihiko Yamashita, Masamitsu Hatakenaka.
South-1, West-16, Chuo-ku, Sapporo, Hokkaido 0608543, Japan

Introduction

Spinal instability (SI), including lumbar degenerative spondylolisthesis, is known as causes of lumbar spinal stenosis and low back pain. Symptomatic patients of SI would require spinal fusion in addition to decompression surgery. SI mainly results from degeneration of intervertebral discs (IVDs) as an anterior supporting mechanism and degeneration of the facet joints as the posterior supporting mechanism. Although performing X-rays with patients in the forward and backward bending posture remains the most common method to assess sagittal instability, this has some disadvantages, including dependence on patient condition.

Most of IVDs with SI show low signal intensities on T2 weighted images because of advanced degeneration of IVD. Previous studies have reported a quantitative evaluation for IVD degeneration using T2. However, advanced degeneration of IVD was difficult to evaluate due to short T2. Meanwhile, ultra-short TE (UTE) technique enables to visualize tissues with short T2 and also to calculate T2* using multi-echoes.

We performed this study was to evaluate T2* obtained from UTE as a potential biomarker with respect to degenerative changes of IVD by comparing T2* between IVDs with and without SI.

Materials and Methods

The study included 11 patients (75.6 ± 8.6 years) with SI and 10 patients (77.3 ± 6.1 years) without SI underwent dynamic radiographs and lumbar MRI as preoperative exams. SI was evaluated by measuring vertebral translation and the degree of angular displacement on dynamic radiograph. MR exams were performed with 3-Tesla system (Ingenia, Philips Healthcare). 3D UTE multi-echo sequence with fat suppression was acquired and T2* was calculated with all TE images (TE = 0.16, 4.6, 9.2, 13.8 ms). We compared T2* of IVDs between with and without SI.

Results

T2* of IVDs with and without SI were 8.27 ± 2.42 and 19.7 ± 10.2 ms, respectively. The T2* of IVDs with SI was significantly lower than that without SI ($p < 0.001$).

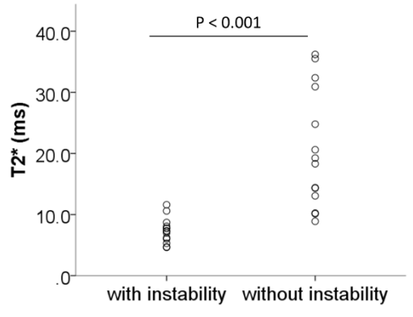

Conclusion

T2* of IVDs obtained by using UTE has a potential as a new biomarker for evaluating IVD degeneration.

Is pleural effusion physiological in DCIS patients on breast MRI?

Minoru Yabuta[1], Hiroko Tsunoda[1], Tomohiro Ochi[2], Yasuyuki Kurihara[1], Hideko Yamauchi[2]

1 Department of Radiology, St. Luke's International Hospital, Tokyo, Japan
2 Department of Breast Surgery, St. Luke's International Hospital, Tokyo, Japan

OBJECTIVE:
To retrospectively evaluate the incidence, side and volume of pleural effusions on breast MRI in DCIS patients proven by surgery.

MATERIALS AND METHODS:
In 128 patients diagnosed as DCIS by surgery between January 2016 and December 2016, medical chart and breast MRI were reviewed. Patients with histories of a prior malignancy, liver, cardiac or pulmonary disease were excluded. To estimate the volume of pleural effusion, the maximal short length of effusions was measured at the anterior chest wall on breast MRI. The incidence and volume of pulmonary effusion, and the correlation in the sides of pleural effusion and DCIS were analyzed.

RESULTS:
Of the 128 patients, 62 (48.4%) had a pleural effusion. Twenty six patients (20.3%) had bilateral pulmonary effusion, and 36 (28.1%) had unilateral. Left-sided pleural effusion was seen in 14 patients, and right-sided in 22 patients. The volume of effusion ranged from 0.1 to 11.0 mm (mean, 3mm). The side of DCIS did not significantly correlate with that of pleural effusion (κ =0.024).

CONCLUSION:
A small amount of pleural effusion is a common finding in DCIS patients. No significant correlation in the sides of pleural effusion and DCIS was noted.

CLINICAL IMPLICATIONS
A small amount of pleural effusion might be physiological on breast MRI

Next symposium in SJRS will be hosted in Sapporo

by Professor Masamitsu Hatakenaka,

President of Progress in Radiology 2020

We look forward to meet again in beautiful Japan!